

Two-Component Algebraic Diagrammatic Construction Theory of Charged Excitations With Consistent Treatment of Spin–Orbit Coupling and Dynamic Correlation

Rajat Majumder[†] and Alexander Yu. Sokolov^{†*}

[†]*Department of Chemistry and Biochemistry, The Ohio State University, Columbus, Ohio 43210, USA*

E-mail: sokolov.8@osu.edu

Abstract

We present a two-component formulation of algebraic diagrammatic construction theory for simulating spin–orbit coupling and electron correlation in charged electronic states and photoelectron spectra. Our implementation supports Hartree–Fock and multiconfigurational reference wavefunctions, enabling efficient correlated calculations of relativistic effects using single-reference (SR-) and multireference (MR-) ADC. We combine the SR- and MR-ADC methods with three flavors of spin–orbit two-component Hamiltonians and benchmark their performance for a variety of atoms and small molecules. When multireference effects are not important, the SR-ADC approximations are competitive in accuracy to MR-ADC, often showing closer agreement with experimental results. However, for electronic states with multiconfigurational character and in non-equilibrium regions of potential energy surfaces, the MR-ADC methods are more reliable, predicting accurate excitation energies and zero-field splittings. Our results demonstrate that the two-component ADC methods are promising approaches for interpreting and predicting the results of modern spectroscopies.

1 Introduction

Charged excitations are perturbations to a chemical system that result in the net change of electron number and charge state. Detailed understanding of these processes is crucial to advancing several key areas, such as developing better photoredox catalysts and semiconductor materials,^{1–3} improving atmospheric and combustion models,^{4,5} and characterizing radiation damage in biomolecules.^{6–8} Charged excitations are also the primary electronic transitions studied in photoelectron spectroscopy that uses high-energy light (UV, XUV, or X-ray) to measure electron binding energies.^{9–11} Recent developments in time-resolved photoelectron spectroscopy enable probing the dynamics of charged electronic states and emitted electrons with atto- and femtosecond time resolution.^{12–15}

Understanding the electronic structure and dynamics of charged excited states requires insights from accurate theoretical calculations. However, simulating charged excitations faces many difficulties associated with the description of orbital re-

laxation, charge localization, and electronic spin. To accurately capture these properties, a variety of electronic structure methods that incorporate electron correlation starting with a single- or multireference wavefunction are available. These approaches range from lower-cost response^{16–27} and perturbation theories^{28–42} to more computationally expensive and accurate configuration interaction^{43–47} and coupled cluster methods.^{48–58}

In addition to electron correlation, simulating charged excitations may require taking into account spin–orbit coupling. Along with scalar relativistic effects, spin–orbit interactions are important for excitations from core *p*- and *d*-orbitals and are critical to the electronic structure of molecules with heavy elements. Accurate treatment of electron correlation and relativistic effects can be achieved using four-component theories based on the Dirac–Coulomb (DC) or Dirac–Coulomb–Breit (DCB) Hamiltonians.^{59–62} However, the computational costs of four-component methods are significantly higher than those of nonrelativistic electronic structure theories, limiting the scope of their applications.

A more economical strategy to simultaneously capture electron correlation and spin-orbit coupling is offered by the two-component relativistic theories. These approaches are formulated by decoupling the electronic and positronic states in the Dirac equation and using the resulting two-component Hamiltonian to describe electron correlation. Two-component methods can be broadly divided into two classes: (i) variational, which introduce spin-orbit interactions in the reference wavefunction,^{61–71} or (ii) perturbative, which first calculate a spin-free relativistic reference wavefunction and incorporate dynamic correlation with spin-orbit coupling *a posteriori*.^{72–78} Most perturbative two-component theories treat spin-orbit coupling as a first-order perturbation and describe dynamic correlation at a higher level of theory. While the first-order approximation is accurate for compounds with light elements at low excitation energies, it is unreliable for electronic states with strong relativistic effects.⁷⁹

In this work, we present an efficient two-component approach for simulating charged excitations that (i) captures static correlation in frontier molecular orbitals, (ii) treats dynamic correlation and spin-orbit coupling as equal perturbations to the nonrelativistic Hamiltonian, and (iii) incorporates their effects in excitation energies and transition intensities up to the second order in perturbation theory. Our approach is formulated in the framework of multireference algebraic diagrammatic construction theory (MR-ADC)^{80,81} that allows to efficiently simulate neutral and charged excitations by approximating linear response functions using low-order multireference perturbation theory.^{82–88} Four-component implementations of single-reference ADC (SR-ADC)^{89–99} with the variational treatment of spin-orbit effects and perturbative description of dynamic correlation in charged^{100–103} and neutral excitations^{104–106} have been reported.

Here, we implement and benchmark the two-component MR-ADC methods for simulating electron-attached (EA) and ionized (IP) states incorporating dynamic correlation and spin-orbit coupling effects up to the second order in perturbation theory. The spin-orbit interactions are described using the Breit-Pauli (BP),^{107–109} first-order Douglas-Kroll-Hess (DKH1), and second-order Douglas-Kroll-Hess Hamiltonians (DKH2)^{110–113} within the mean-field spin-orbit approximation.^{109,111–114} The DKH1 and DKH2

Hamiltonians were formulated using the exact two-component approach developed by Liu and co-workers.^{110,111} Starting with a single-determinant (Hartree-Fock) reference wavefunction, our two-component MR-ADC methods reduce to the two-component SR-ADC approximations, for which results are also presented.

2 Theory

2.1 Algebraic Diagrammatic Construction Theory of Charged Excitations

Algebraic diagrammatic construction (ADC) belongs to a class of propagator theories that describe charged excitations in terms of the one-particle Green’s function (1-GF).^{89–99} For the N -electron reference electronic state $|\Psi^N\rangle$ with energy E_N (usually, the ground state), 1-GF can be expressed as

$$\begin{aligned} G_{pq}(\omega) &= G_{pq}^+(\omega) + G_{pq}^-(\omega) \\ &= \langle \Psi^N | a_p(\omega - H + E_N)^{-1} a_q^\dagger | \Psi^N \rangle \\ &\quad + \langle \Psi^N | a_q^\dagger(\omega + H - E_N)^{-1} a_p | \Psi^N \rangle \end{aligned} \quad (1)$$

where $G_{pq}^+(\omega)$ and $G_{pq}^-(\omega)$ are the forward and backward components of 1-GF, H is the electronic Hamiltonian, and ω is the frequency of radiation promoting the charged excitations. The a_p^\dagger/a_p are the creation/annihilation operators describing electron addition/removal. Alternatively, 1-GF can be written in a spectral representation

$$\begin{aligned} G_{pq}(\omega) &= \sum_n \frac{\langle \Psi^N | a_p | \Psi_n^{N+1} \rangle \langle \Psi_n^{N+1} | a_q^\dagger | \Psi^N \rangle}{\omega - E_{N+1,n} + E_N} \\ &\quad + \sum_n \frac{\langle \Psi^N | a_q^\dagger | \Psi_n^{N-1} \rangle \langle \Psi_n^{N-1} | a_p | \Psi^N \rangle}{\omega + E_{N-1,n} - E_N} \end{aligned} \quad (2)$$

that encodes information about the vertical electron affinities ($E_{N+1,n} - E_N$), ionization energies ($E_{N-1,n} - E_N$), and the corresponding transition probabilities ($\langle \Psi^N | a_p | \Psi_n^{N+1} \rangle \langle \Psi_n^{N+1} | a_q^\dagger | \Psi^N \rangle$ and $\langle \Psi^N | a_q^\dagger | \Psi_n^{N-1} \rangle \langle \Psi_n^{N-1} | a_p | \Psi^N \rangle$).

ADC approximates the exact 1-GF by expressing each term in Eq. (2) as a product of non-diagonal matrices:

$$\mathbf{G}_\pm(\omega) = \mathbf{T}_\pm(\omega \mathbf{S}_\pm - \mathbf{M}_\pm)^{-1} \mathbf{T}_\pm \quad (3)$$

Here, \mathbf{M}_\pm and \mathbf{T}_\pm are the effective Hamiltonian and transition moments matrices that provide in-

formation about vertical charged excitation energies and transition probabilities, respectively. Each matrix is expressed in a basis of $(N \pm 1)$ -electron excited-state configurations that are, in general, nonorthogonal with overlap integrals stored in \mathbf{S}_\pm . Approximating \mathbf{M}_\pm , \mathbf{T}_\pm , and \mathbf{S}_\pm using perturbation theory up to the order n

$$\mathbf{M}_\pm \approx \mathbf{M}_\pm^{(0)} + \mathbf{M}_\pm^{(1)} + \dots + \mathbf{M}_\pm^{(n)} \quad (4)$$

$$\mathbf{T}_\pm \approx \mathbf{T}_\pm^{(0)} + \mathbf{T}_\pm^{(1)} + \dots + \mathbf{T}_\pm^{(n)} \quad (5)$$

$$\mathbf{S}_\pm \approx \mathbf{S}_\pm^{(0)} + \mathbf{S}_\pm^{(1)} + \dots + \mathbf{S}_\pm^{(n)} \quad (6)$$

defines the n th-order ADC approximation (ADC(n)).

Diagonalizing the \mathbf{M}_\pm matrices allows to compute charged excitation energies (Ω_\pm):

$$\mathbf{M}_\pm \mathbf{Y}_\pm = \mathbf{S}_\pm \mathbf{Y}_\pm \Omega_\pm \quad (7)$$

The corresponding eigenvectors \mathbf{Y}_\pm can be combined with the transition moments matrices \mathbf{T}_\pm to compute spectroscopic amplitudes

$$\mathbf{X}_\pm = \mathbf{T}_\pm \mathbf{S}_\pm^{-1/2} \mathbf{Y}_\pm \quad (8)$$

which provide information about the probabilities of charged excitations.

2.2 Multireference ADC

Two ADC formulations have been proposed: single-reference (SR-) ^{89–99,115,116} and multireference (MR-) ^{80–88} ADC. In SR-ADC, contributions to \mathbf{M}_\pm , \mathbf{T}_\pm , and \mathbf{S}_\pm are evaluated using Møller–Plesset perturbation theory ¹¹⁷ following a Hartree–Fock calculation for the reference state (Figure 1a). MR-ADC starts with a complete active space self-consistent field (CASSCF, Figure 1b) reference wavefunction $|\Psi_0\rangle$ and incorporates dynamic correlation effects using multireference N -electron valence perturbation theory. ^{36,118,119} If the number of active orbitals in the CASSCF reference wavefunction is zero, the MR-ADC(n) methods reduce to the SR-ADC(n) approximations.

Perturbative contributions to the MR-ADC(n)

matrices in Eqs. (4) to (6) can be expressed as: ^{82,83}

$$M_{+\mu\nu}^{(n)} = \sum_{klm}^{k+l+m=n} \langle \Psi_0 | [h_{+\mu}^{(k)}, [\tilde{H}^{(l)}, h_{+\nu}^{(m)\dagger}]]_+ | \Psi_0 \rangle \quad (9)$$

$$T_{+p\nu}^{(n)} = \sum_{kl}^{k+l=n} \langle \Psi_0 | [\tilde{a}_p^{(k)}, h_{+\nu}^{(l)\dagger}]_+ | \Psi_0 \rangle \quad (10)$$

$$S_{+\mu\nu}^{(n)} = \sum_{kl}^{k+l=n} \langle \Psi_0 | [h_{+\mu}^{(k)}, h_{+\nu}^{(l)\dagger}]_+ | \Psi_0 \rangle \quad (11)$$

$$M_{-\mu\nu}^{(n)} = \sum_{klm}^{k+l+m=n} \langle \Psi_0 | [h_{-\mu}^{(k)\dagger}, [\tilde{H}^{(l)}, h_{-\nu}^{(m)}]]_+ | \Psi_0 \rangle \quad (12)$$

$$T_{-p\nu}^{(n)} = \sum_{kl}^{k+l=n} \langle \Psi_0 | [\tilde{a}_p^{(k)}, h_{-\nu}^{(l)}]_+ | \Psi_0 \rangle \quad (13)$$

$$S_{-\mu\nu}^{(n)} = \sum_{kl}^{k+l=n} \langle \Psi_0 | [h_{-\mu}^{(k)\dagger}, h_{-\nu}^{(l)}]_+ | \Psi_0 \rangle \quad (14)$$

Here, $[A, B] = AB - BA$ denotes a commutator, $[A, B]_+ = AB + BA$ is an anticommutator, while $\tilde{H}^{(k)}$, $\tilde{a}_p^{(k)}$, and $h_{\pm\nu}^{(k)\dagger}$ are the k th-order contributions to effective Hamiltonian (\tilde{H}), effective observable (\tilde{a}_p), and excitation manifold ($h_{\pm\nu}^\dagger$) operators, respectively.

The low-order $\tilde{H}^{(k)}$ and $\tilde{a}_p^{(k)}$ have the form: ^{82,83}

$$\tilde{H}^{(0)} = H^{(0)} \quad (15)$$

$$\tilde{H}^{(1)} = V + [H^{(0)}, T^{(1)} - T^{(1)\dagger}] \quad (16)$$

$$\tilde{H}^{(2)} = [H^{(0)}, T^{(2)} - T^{(2)\dagger}] + \frac{1}{2} [V + \tilde{H}^{(1)}, T^{(1)} - T^{(1)\dagger}] \quad (17)$$

$$\tilde{a}_p^{(0)} = a_p \quad (18)$$

$$\tilde{a}_p^{(1)} = [a_p, T^{(1)} - T^{(1)\dagger}] \quad (19)$$

$$\tilde{a}_p^{(2)} = [a_p, T^{(2)} - T^{(2)\dagger}] + \frac{1}{2} [[a_p, T^{(1)} - T^{(1)\dagger}], T^{(1)} - T^{(1)\dagger}] \quad (20)$$

where $H^{(0)}$ is the Dyal zeroth-order Hamiltonian, ¹²⁰ $V = H - H^{(0)}$ is the perturbation operator, and $T^{(k)}$ is the k th-order cluster correlation operator. The Dyal Hamiltonian $H^{(0)}$ incorporates the one- and two-electron active-space terms of the electronic Hamiltonian H and describes the static electron correlation in active orbitals. ⁸¹ The V and $T^{(k)}$ operators incorporate dynamic correlation in non-active orbitals. Up to the second order in multireference perturbation theory, $T^{(k)}$ ($k \leq 2$) incorporates single and double excitations out of

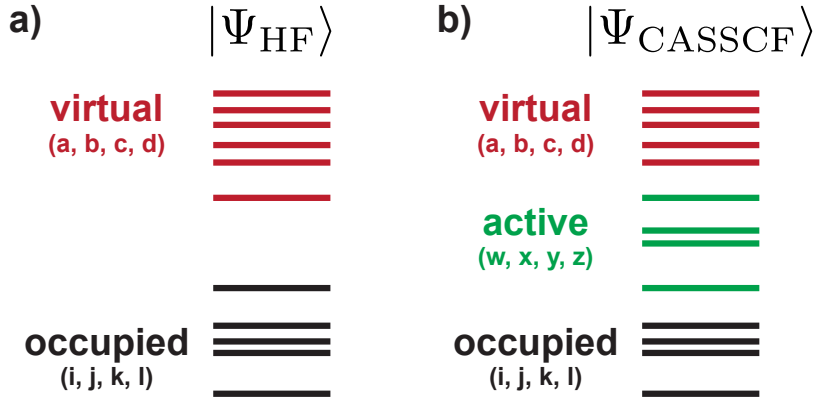


Figure 1: Schematic diagram representing molecular orbitals and their labels for a) the Hartree-Fock (HF) reference wavefunction in SR-ADC and (b) the CASSCF reference wavefunction in MR-ADC. Reproduced from Ref. 98 with permission from the American Chemical Society. Copyright 2023.

the reference wavefunction $|\Psi_0\rangle$ and can be written as

$$T^{(k)} = \sum_{\mu} t_{\mu}^{(k)} \tau_{\mu}^{\dagger} \quad (21)$$

where the amplitudes $t_{\mu}^{(k)}$ are determined by projecting the k th-order effective Hamiltonian on the singly and doubly excited configurations $\tau_{\mu}^{\dagger}|\Psi_0\rangle$:^{82,83}

$$\langle\Psi_0|\tau_{\mu}\tilde{H}^{(k)}|\Psi_0\rangle = 0 \quad (22)$$

Finally, the excitation manifold operators $h_{\pm\nu}^{(k)\dagger}$ are used to represent $\tilde{H}^{(k)}$ and $\tilde{a}_p^{(k)}$ in Eqs. (9) to (13) in the basis of $(N \pm 1)$ -electron electronic configurations $(h_{\pm\nu}^{(k)\dagger}|\Psi_0\rangle)$.^{82,83} These multireference wavefunctions are depicted in Figure 2 for $k = 0$ and 1. The $h_{\pm\nu}^{(0)\dagger}$ operators incorporate all $(N \pm 1)$ -electron excitations in the active space ($|\Psi_{\pm I}\rangle$) together with the one-electron attachment/ionization in virtual/core orbitals ($|\Psi^a\rangle/|\Psi_i\rangle$), respectively. The charged excitations out of active space involving two electrons are described by $h_{\pm\nu}^{(1)\dagger}$.

Eqs. (9) to (13) define the perturbative structure of MR-ADC(n) matrices where the sum of orders for $h_{\pm\nu}^{(k)\dagger}$, $\tilde{H}^{(l)}$, and $\tilde{a}_p^{(m)}$ cannot exceed n for a particular matrix element. Figure 3 illustrates this for the low-order MR-ADC methods. In addition to the strict MR-ADC(0), MR-ADC(1), and MR-ADC(2) approximations, an extended second-order MR-ADC method (MR-ADC(2)-X) has been developed, which incorporates higher-order terms in \mathbf{M}_{\pm} and \mathbf{T}_{\pm} for the description of double excitations $(h_{\pm\nu}^{(1)\dagger})$.⁸³ Keeping the size of active space constant, MR-ADC(2) and MR-ADC(2)-X have

the $\mathcal{O}(N^5)$ computational scaling with the basis set size (N), which allows to perform calculations for molecules with more than 1000 molecular orbitals.⁸⁸

2.3 Incorporating Relativistic Effects in MR-ADC

The goal of this work is to incorporate relativistic effects in the MR-ADC calculations of charged electronic states without significantly increasing their computational cost. To achieve this, we employ three variants of two-component relativistic Hamiltonians, namely: Breit-Pauli (BP),^{107–109} first-order Douglas-Kroll-Hess (DKH1),^{110,111} and second-order Douglas-Kroll-Hess (DKH2).¹¹¹ These Hamiltonians are derived by approximately decoupling the electronic and positronic degrees of freedom in the four-component Dirac equation and subsequently adding the Coulomb and Gaunt two-electron terms. The BP Hamiltonian represents the lowest level of decoupling, which is valid when relativistic effects are weak but becomes increasingly inaccurate as these effects get stronger. The DKH1 and DKH2 Hamiltonians used in this work are formulated using the spin-free exact two-component approach of Liu and co-workers (X2C-1e),¹¹⁰ which provides a more accurate description of scalar relativistic terms than BP and conventional DKH Hamiltonians.^{63,121,122} We refer the readers to excellent reviews on this topic for additional information.^{61,66,123}

Each two-component Hamiltonian can be expressed in a general form as:

$$H_{2c} = H_{\text{SF}} + H_{\text{SO}} \quad (23)$$

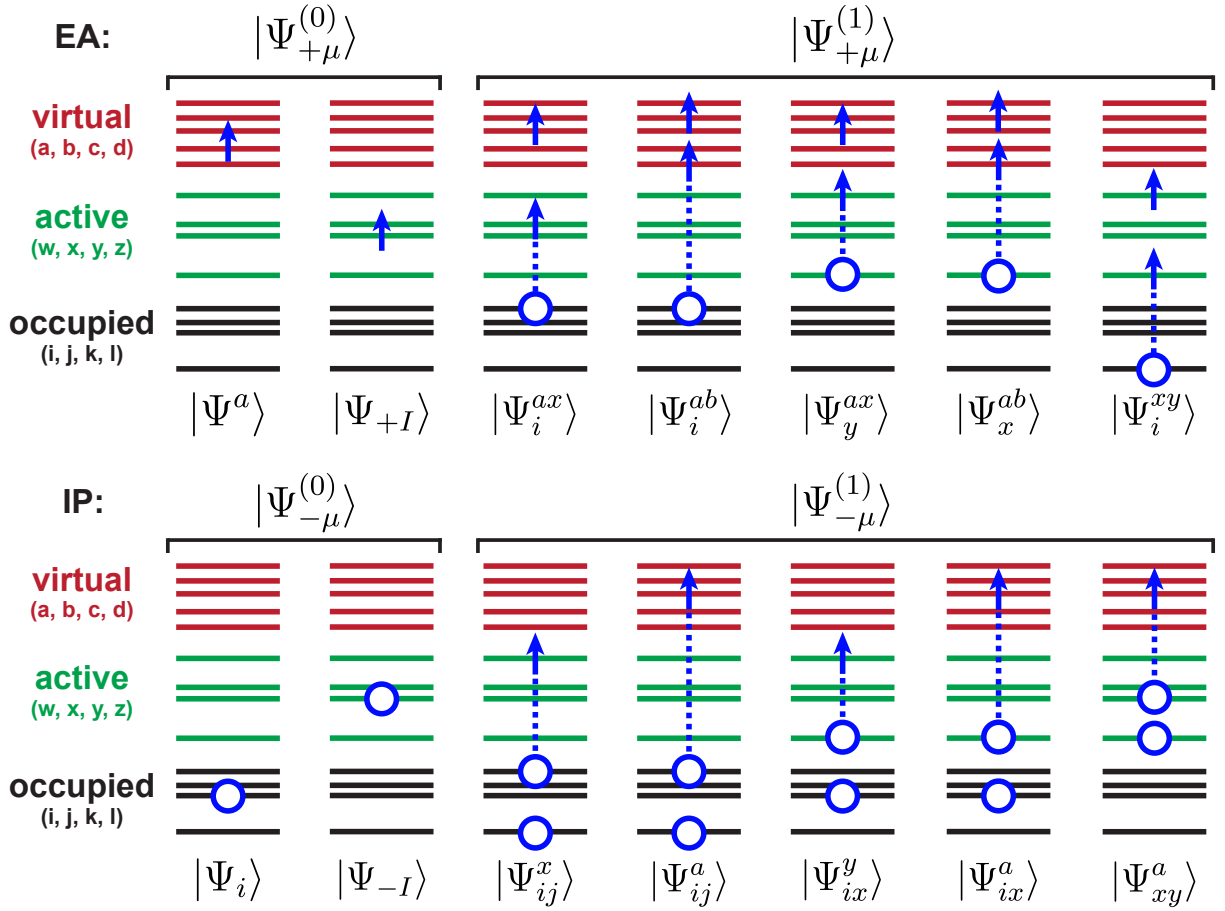


Figure 2: Schematic illustration of the electron-attached and ionized states produced by acting the $h_{\pm\mu}^{(k)\dagger}$ ($k = 0, 1$) operators on the reference state $|\Psi_0\rangle$ in MR-ADC(2) and MR-ADC(2)-X. An arrow represents electron attachment, a circle denotes ionization, and a circle connected with an arrow indicates single excitation. The states $|\Psi_{\pm I}\rangle$ incorporate all $(N \pm 1)$ -electron excitations in the active orbitals. Reproduced from Ref. 98 with permission from the American Chemical Society. Copyright 2023.

		$ \Psi_{\pm\nu}^{(0)}\rangle$	$ \Psi_{\pm\nu}^{(1)}\rangle$	$ \Psi_{\pm\nu}^{(0)}\rangle$	$ \Psi_{\pm\nu}^{(1)}\rangle$	$ \Psi_{\pm\nu}^{(0)}\rangle$	$ \Psi_{\pm\nu}^{(1)}\rangle$	$ \Psi_{\pm\nu}^{(0)}\rangle$	$ \Psi_{\pm\nu}^{(1)}\rangle$
M :	$\langle\Psi_{\pm\mu}^{(0)} $	0		1		2	1	2	1
	$\langle\Psi_{\pm\mu}^{(1)} $					1	0	1	1
T :	p	0		1		2	1	2	2
		ADC(0)		ADC(1)		ADC(2)		ADC(2)-X	

Figure 3: Perturbative structures of the effective Hamiltonian (\mathbf{M}_{\pm}) and transition moments (\mathbf{T}_{\pm}) matrices in the low-order MR-ADC approximations. Numbers denote the perturbation order to which the effective Hamiltonian and transition moments are expanded for each sector. Shaded areas indicate nonzero blocks. Adapted from Ref. 98 with permission from the American Chemical Society. Copyright 2023.

where H_{SF} describes the scalar relativistic effects and H_{SO} incorporates spin-orbit coupling. For

BP and DKH1, we choose H_{SF} to be the X2C-1e Hamiltonian¹¹⁰ that captures the scalar relativistic

effects more accurately than the spin-free contributions of the conventional BP and DKH1 Hamiltonians ($H_{\text{SF}} = H_{\text{SF}}^{\text{X2C}^{-1\text{e}}}$). For DKH2, H_{SF} is defined as the X2C-1e Hamiltonian plus additional terms from the second-order DKH transformation due to the picture change effect ($H_{\text{SF}} = H_{\text{SF}}^{\text{X2C}^{-1\text{e}}} + H_{\text{SF}}^{\text{DKH2}}$). Working equations for $H_{\text{SF}}^{\text{X2C}^{-1\text{e}}}$ and $H_{\text{SF}}^{\text{DKH2}}$ can be found in Ref. 111.

Within the spin-orbit mean-field approximation (SOMF),^{109,114} the BP, DKH1, and DKH2 spin-dependent Hamiltonians can be written in a general form:^{108–111}

$$H_{\text{SO}} = i \frac{\alpha^2}{4} \sum_{\xi} \sum_{pq} F_{pq}^{\xi} D_{pq}^{\xi} \quad (24)$$

where $\alpha = 1/c$ is the fine-structure constant, the indices (p, q, \dots) label all spatial molecular orbitals in the one-electron basis set, $\xi = x, y, z$ denotes Cartesian coordinates, and D_{pq}^{ξ} are the one-electron spin excitation operators

$$D_{pq}^x = a_{p\alpha}^{\dagger} a_{q\beta} + a_{p\beta}^{\dagger} a_{q\alpha} \quad (25)$$

$$D_{pq}^y = i(a_{p\beta}^{\dagger} a_{q\alpha} - a_{p\alpha}^{\dagger} a_{q\beta}) \quad (26)$$

$$D_{pq}^z = a_{p\alpha}^{\dagger} a_{q\alpha} - a_{p\beta}^{\dagger} a_{q\beta} \quad (27)$$

with α and β denoting the spin-up and spin-down electrons, respectively. The expressions for the matrix elements F_{pq}^{ξ} of each two-component Hamiltonian can be found in Ref. 79.

In our formulation of two-component MR-ADC, we incorporate the scalar relativistic effects in the reference CASSCF calculation by including H_{SF} in the zeroth-order Hamiltonian

$$H_{2c}^{(0)} = H^{(0)} + H_{\text{SF}} \quad (28)$$

To describe spin-orbit coupling, we define a new perturbation operator

$$V_{2c} = V + H_{\text{SO}} = H - H^{(0)} + H_{\text{SO}} \quad (29)$$

where V captures dynamic correlation in non-active orbitals (Section 2.2) and the two component spin-orbit operator H_{SO} is defined in Eq. (24). Replacing $H^{(0)}$ by $H_{2c}^{(0)}$ and V by V_{2c} in Eqs. (15) to (20) allows to formulate the two-component MR-ADC(n) methods with consistent perturbative treatment of dynamic correlation and spin-orbit coupling effects.

Incorporating H_{SO} requires several changes in the MR-ADC implementation:

1. H_{SO} modifies the amplitudes of correlation operator $T^{(k)}$ (Eq. (21)) by entering the amplitude equations (22) for the single and semi-internal double excitations. Following the standard NEVPT2 notation,³⁶ these amplitudes belong to the $[\pm 1']$ and $[0']$ excitation classes and can be denoted as $t_i^{a(k)}$, $t_i^{x(k)}$, $t_x^{a(k)}$, $t_{ix}^{ay(k)}$, $t_{ix}^{yz(k)}$, and $t_{xy}^{az(k)}$ using the orbital index labels in Figure 1. Due to the SOMF approximation, the amplitude equations for other excitation classes remain unaffected. As in our nonrelativistic implementation,^{82,83} the second order correlation operator $T^{(2)}$ has negligible contributions to the MR-ADC matrices up to the MR-ADC(2)-X level of theory. For this reason, we include only one class of second-order correlation amplitudes ($t_i^{a(2)}$) to ensure consistency with the single-reference ADC approximations.
2. Since H_{SO} contains terms with all active indices, a new class of internal single excitations ($t_x^{y(1)}$, $x > y$) is introduced. These correlation amplitudes are necessary to account for the active-space spin-orbit coupling effects in the reference wavefunction and to ensure that the effective Hamiltonian matrix \mathbf{M}_{\pm} is complex-Hermitian. For additional details and derivation of $t_x^{y(1)}$ amplitude equations, we refer the readers to the Appendix.
3. Finally, the spin-orbit contributions to $T^{(k)}$ and V modify the \mathbf{M}_{\pm} and \mathbf{T}_{\pm} matrix elements. Implementation of these new contributions requires properly treating complex conjugation and permutational symmetry of complex-valued tensors.

Table 1 summarizes the capabilities of our two-component MR-ADC implementation, which allows to calculate electron-attached (EA) and ionized (IP) states using three variants of relativistic Hamiltonians (BP/DKH1/DKH2) up to the MR-ADC(2)-X level of theory. Our implementation supports both CASSCF and restricted Hartree-Fock (RHF) reference wavefunctions and can be used to perform two-component SR-ADC calculations for molecules with a closed-shell reference state. Although the MR-ADC(n) methods developed in this work are perturbative in nature, they deliver the exact energies of SOMF

Table 1: Two-component SR- and MR-ADC methods implemented in this work. X2C-1e stands for the spin-free (SF) exact two-component approach of Liu and co-workers.¹¹⁰ For the discussion of spin-orbit (SO) Hamiltonians and other details see Section 2.3.

Method	SF Hamiltonian	SO Hamiltonian
BP-(EA/IP)-(SR/MR)ADC(2)	X2C-1e	BP
BP-(EA/IP)-(SR/MR)ADC(2)-X	X2C-1e	BP
DKH1-(EA/IP)-(SR/MR)ADC(2)	X2C-1e	DKH1
DKH1-(EA/IP)-(SR/MR)ADC(2)-X	X2C-1e	DKH1
DKH2-(EA/IP)-(SR/MR)ADC(2)	X2C-1e + DKH2	DKH2
DKH2-(EA/IP)-(SR/MR)ADC(2)-X	X2C-1e + DKH2	DKH2

BP/DKH1/DKH2 Hamiltonian when all orbitals are included in the active space starting with the first-order approximation ($n \geq 1$). Our current implementation is restricted to non-degenerate reference states due to the state-specific nature of correlation amplitudes determined from Eq. (22). A generalization of this approach to degenerate reference states will be reported in a forthcoming publication.

In the following sections, we present a benchmark study of the relativistic ADC methods, starting with a brief summary of computational details.

3 Computational details

The two-component EA/IP-ADC methods were implemented in the development version of PRISM.¹²⁴ All one- and two-electron integrals and the CASSCF reference wavefunctions were computed using PYSCF.¹²⁵ The matrix elements of DKH1 Hamiltonian were computed by interfacing PRISM with SOCUTILS.^{113,126} The DKH2 matrix elements were implemented in a local version of SOCUTILS.⁷⁹

We performed four sets of benchmark calculations. In Section 4.1, we assess the accuracy of two-component EA/IP-ADC methods for predicting zero-field splitting in the 2P and $^2\Pi$ states of main group atoms and diatomics. Next, in Section 4.2, we carry out benchmark calculations for the transition metal atoms with d^1 and d^9 electronic configurations. In Section 4.3, we simulate the photoelectron spectra of cadmium halides (CdX_2 , $X = \text{Cl, Br, I}$) using the IP-ADC methods. Finally, in Section 4.4, we compute the photoelectron spectra of methyl iodide (CH_3I) at equilibrium and along the C–I bond dissociation.

All electrons were correlated in all ADC calculations. For an open-shell system containing N

electrons, the EA/IP-ADC results were computed starting with the $(N \mp 1)$ -electron lowest-energy singlet reference state. The geometries, active spaces, and CASCI states ($|\Psi_{\pm I}\rangle$ in Figure 2) chosen for each calculation are provided in the Supplementary Information. The MR-ADC calculations were performed using the $\eta_s = 10^{-5}$ and $\eta_d = 10^{-10}$ parameters to remove linearly dependent semiinternal and double excitations, respectively.^{82,83}

For the main group elements and diatomics (Section 4.1), we utilized the ANO-RCC-VTZP basis set.¹²⁷ The diatomic bond lengths were set to their experimental values,¹²⁸ which are provided in the Supplementary Information. The calculations of transition metal atoms with the d^1 and d^9 electronic configurations (Section 4.2) were performed using the all electron X2C-TZVPall-2c basis set.¹²⁹ To compute the photoelectron spectra of cadmium halides (Section 4.3), we employed the X2C-QZVPall basis set¹³⁰ and structural parameters from Ref. 131. The CdX_2 experimental photoelectron spectra were digitized using the WebPlot-Digitizer¹³² from the data reported in Refs. 133 and 134.

Finally, for the simulations of CH_3I photoelectron spectra (Section 4.4) we used the X2C-TZVPall basis set.¹²⁹ The CH_3I equilibrium geometry was optimized using density functional theory with the B3LYP functional¹³⁵ and the def2-TZVP basis set.^{136,137} The reference CASSCF wavefunctions were calculated for the lowest-energy singlet state incorporating 6 electrons in 7 active orbitals (6e, 7o), which included the lone pairs of the iodine atom, the σ -bonding and antibonding C–I orbitals, and three more antibonding orbitals localized on the CH_3 group. Photoelectron spectra were simulated for the equilibrium, stretched, and completely dissociated CH_3I structures. In the stretched ge-

ometry, the C–I bond was elongated by a factor of two relative to its equilibrium value (r_e), keeping the structure of CH₃ group frozen (pyramidal). For the dissociated geometry (CH₃+I), the C–I distance was set to ~ 6.7 Å and the CH₃ fragment was fully optimized at the CCSD(T)/def2-TZVP level of theory in a separate calculation without the I atom being present. These geometries are reported in the Supplementary Information.

4 Results and Discussion

4.1 Zero-field splitting in main group atoms and diatomics

We begin with a benchmark of two-component ADC approximations for calculating the zero-field splitting (ZFS) in main group atoms and diatomic molecules that do not exhibit multireference effects. Tables 2 and 3 compare the results of EA-ADC methods with available experimental data^{112,139} for the group 1 and 13 atoms and group 2 and 14 hydrides. The IP-ADC benchmark calculations (Tables 4 and 5) were performed for the group 17 atoms, group 18 cations, as well as group 16 neutral and group 17 cationic hydrides. For an atom or molecule with N electrons, the EA/IP-ADC calculations were performed for the lowest-energy term of 2P or $^2\Pi$ symmetry starting with the $(N \mp 1)$ singlet reference wavefunction. Additional computational details can be found in Section 3 and the Supporting Information.

The benchmark results are summarized in Figure 4 and Table 6 where the EA/IP-ADC mean absolute errors (MAE) in % and cm^{-1} are calculated relative to the experimental data for each row of periodic table. For the second- and third-period elements, the computed ZFS show little dependence on the choice of two-component spin-orbit Hamiltonian (BP, DKH1, and DKH2). Starting with the fourth period, the BP-ADC methods deteriorate in accuracy and exhibit convergence problems in the iterative diagonalization of effective Hamiltonian matrix. The DKH1- and DKH2-ADC calculations do not experience convergence issues and are significantly more accurate compared to BP-ADC for heavier elements.

To compare the accuracy of ADC levels of theory in predicting the ZFS of main group elements, we focus on the DKH2 results in Figure 4 and Table 6. For periods 2 and 3, all DKH2-EA-ADC methods show similar accuracy with MAE of ~ 1

and 3 cm^{-1} , which represents ~ 5 to 10 % error relative to experimental ZFS due to weak spin-orbit coupling in these systems. In periods 4 and 5, the DKH2-EA-ADC MAE range from 16 to 39 cm^{-1} (2.6 to 11.3 %) and from 132 to 220 cm^{-1} (5.8 to 15.5 %), respectively. Since the molecules in this benchmark set do not exhibit multireference effects, the EA-SR-ADC methods are competitive in accuracy to EA-MR-ADC, often showing better performance. The DKH2-EA-SR-ADC(2) method has the smallest MAE for periods 4 and 5, despite being the lowest level of theory out of four DKH2-EA-ADC approximations.

The DKH2-IP-ADC methods show somewhat larger errors in ZFS compared to DKH2-EA-ADC, which represent a smaller % fraction (~ 2 to 6 %) of the experimental reference data. Going down the periodic table, the DKH2-IP-ADC MAE ranges are $14.9 - 24.5$, $15.3 - 63.8$, $27.3 - 116.1$, and $148.1 - 407.6 \text{ cm}^{-1}$ for periods 2, 3, 4, and 5, respectively (Table 6). The DKH2-IP-SR-ADC(2)-X and DKH2-IP-MR-ADC(2) methods tend to show smaller MAE for periods 4 and 5 within a limited scope of our benchmark study.

4.2 Spin-orbit coupling in d^1 and d^9 transition metal atoms

We now turn our attention to the transition metal atoms with the d^1 (ground-state Sc, Y, La) and d^9 (excited-state Cu, Ag, Au) electronic configurations. Table 7 reports the ZFS in the ground 2D term of Sc, Y, and La atoms computed using the two-component EA-ADC methods starting with the 1S reference states of their cations. Earlier studies using two-component multireference configuration interaction (X2C-MRCISD)⁷¹ and quasidenerate N-electron valence perturbation theory (DKH2-QDNEVPT2)⁷⁹ reported significant errors in the ZFS of these elements (Table 7). For example, the variational X2C-MRCISD method shows the 10.2 and 11.2 % errors in ZFS for Sc and La, respectively. The smallest error in the DKH2-QDNEVPT2 calculations is 14.9 % (La).⁷⁹

For all d^1 atoms (Sc, Y, and La), the EA-SR-ADC and EA-MR-ADC methods show similar results at the same level of spin-orbit and dynamic correlation treatment. The DKH-EA-ADC(2)-X family of methods exhibits the best performance predicting the ZFS of Sc, Y, and La within ~ 21 , 13 , and 4 % of the experimental data,^{139–141} respectively (Table 7). For the La

Table 2: Zero-field splitting (cm^{-1}) in the 2P states of main group atoms and the $^2\Pi$ states of diatomics computed using the two-component EA-MR-ADC methods with the BP, DKH1, or DKH2 spin-orbit Hamiltonians. All calculations employed the uncontracted ANO-RCC-VTZP basis set.

System	BP-EA-MR-ADC(2)	DKH1-EA-MR-ADC(2)	DKH2-EA-MR-ADC(2)	BP-EA-MR-ADC(2)-X	DKH1-EA-MR-ADC(2)-X	DKH2-EA-MR-ADC(2)-X	Experiment ^a
B	13.2	13.2	13.2	13.8	13.8	13.8	15.0
Al	112	112	112	117	116	116	112
Ga	1045	942	949	998	899	906	826
In	^b	2796	2843	^b	2756	2802	2213
Na	13.0	12.9	12.9	13.9	13.8	13.8	17.2
K	43	43	43	55	55	55	58
Rb	^b	237	239	^b	264	267	238
Cs	^b	474	474	^b	584	595	554
CH	26	26	26	26	26	26	28
SiH	135	134	134	138	137	137	143
GeH	1118	894	901	1120	892	900	893
SnH	^b	2304	2344	^b	2361	2402	2178
BeH	1.76	1.76	1.76	1.88	1.88	1.88	2.14
MgH	33	33	33	36	36	36	35
CaH	77	76	76	82	80	81	79
SrH	^b	296	261	^b	259	261	300

^a Experimental results are from Refs. 138 and 139.

^b Convergence problems encountered when using the BP Hamiltonian.

Table 3: Zero-field splitting (cm^{-1}) in the 2P states of main group atoms and the $^2\Pi$ states of diatomics computed using the two-component EA-SR-ADC methods with the BP, DKH1, or DKH2 spin-orbit Hamiltonians. All calculations employed the uncontracted ANO-RCC-VTZP basis set.

System	BP-EA-SR-ADC(2)	DKH1-EA-SR-ADC(2)	DKH2-EA-SR-ADC(2)	BP-EA-SR-ADC(2)-X	DKH1-EA-SR-ADC(2)-X	DKH2-EA-SR-ADC(2)-X	Experiment ^a
B	14.0	14.0	14.3	15.5	16.0	15.4	15.0
Al	111	109	103	109	115	109	112
Ga	937	845	852	981	884	892	826
In	^b	2416	2456	^b	2518	2559	2213
Na	15.5	15.5	15.5	16.1	16.0	16.0	17.2
K	58	57	57	61	60	60	58
Rb	^b	238	240	^b	248	251	238
Cs	^b	585	597	^b	610	623	554
CH	26	26	26	29	29	29	28
SiH	142	140	140	150	149	149	143
GeH	1151	919	927	1214	969	978	893
SnH	^b	2412	2454	^b	2534	2578	2178
BeH	1.74	1.74	1.75	1.85	1.84	1.85	2.14
MgH	34	32	33	34	34	34	35
CaH	83	81	81	86	85	85	79
SrH	^b	291	294	^b	308	311	300

^a Experimental results are from Refs. 138 and 139.

^b Convergence problems encountered when using the BP Hamiltonian.

atom, the DKH-EA-ADC(2)-X methods outperform the X2C-MRCISD approach, likely due to a fortuitous error cancellation. When compared to DKH2-QDNEVPT2, DKH-EA-ADC(2)-X show better results for Y and La. The strict second-order approximations (DKH-EA-ADC(2)) exhibit significantly larger errors than their extended (-X) counterparts (~ 35 , 26 , and 5 % for Sc, Y, and La). As for the main group elements and diatomics (Section 4.1), the BP spin-orbit Hamiltonian produces similar results to DKH1/DKH2 for lighter elements (Sc and Y) but is unreliable for the heavier La atom.

To assess the performance of two-component IP-ADC approximations, we calculated the ZFS of Cu, Ag, and Au atoms in the excited 2D term (d^9 electronic configuration) starting with the lowest-energy closed-shell anionic reference state (Table 8). In contrast to the d^1 atoms, the IP-SR-ADC and IP-MR-ADC ZFS are significantly different, with the multireference approximations showing closer agreement with the experimental data. The DKH-IP-MR-ADC(2)-X methods exhibit the best performance, predicting the ZFS of Cu, Ag, and Au within ~ 1 , 4 , and 6 % of their experimental values, respectively. DKH-IP-MR-ADC(2) yield

Table 4: Zero-field splitting (cm^{-1}) in the 2P states of main group atoms and the $^2\Pi$ states of diatomics computed using the two-component IP-MR-ADC methods with the BP, DKH1, or DKH2 spin-orbit Hamiltonians. All calculations employed the uncontracted ANO-RCC-VTZP basis set.

System	BP-IP-MR-ADC(2)	DKH1-IP-MR-ADC(2)	DKH2-IP-MR-ADC(2)	BP-IP-MR-ADC(2)-X	DKH1-IP-MR-ADC(2)-X	DKH2-IP-MR-ADC(2)-X	Experiment ^a
F	385	384	384	389	388	388	404
Cl	885	873	875	892	880	880	882
Br	4014	3672	3708	^b	3701	3737	3685
I	9980	7533	7661	^b	7593	7722	7603
Ne ⁺	757	754	755	760	757	758	780
Ar ⁺	1417	1395	1256	1425	1403	1410	1432
Kr ⁺	5906	5369	5423	^b	5386	5441	5370
Xe ⁺	12780	9832	9996	^b	9751	9914	10537
Rn ⁺	^b	27208	27654	^b	27388	27842	30895
OH	128	128	128	130	130	130	139
SH	348	344	345	341	337	338	377
SeH	1754	1623	1640	^b	1571	1585	1764
TeH	4294	3438	3492	^b	3335	3386	3816
HF ⁺	279	278	279	281	280	281	293
HCl ⁺	613	605	607	616	608	610	648
HBr ⁺	2717	2502	2525	^b	2490	2513	2653
HI ⁺	6179	4915	4990	^b	4866	4941	5400

^a Experimental results are from Refs. 138 and 139.

^b Convergence problems encountered when using the BP Hamiltonian.

Table 5: Zero-field splitting (cm^{-1}) in the 2P states of main group atoms and the $^2\Pi$ states of diatomics computed using the two-component IP-SR-ADC methods with the BP, DKH1, or DKH2 spin-orbit Hamiltonians. All calculations employed the uncontracted ANO-RCC-VTZP basis set.

System	BP-IP-SR-ADC(2)	DKH1-IP-SR-ADC(2)	DKH2-IP-SR-ADC(2)	BP-IP-SR-ADC(2)-X	DKH1-IP-SR-ADC(2)-X	DKH2-IP-SR-ADC(2)-X	Experiment ^a
F	382	389	381	439	437	438	404
Cl	849	837	840	917	904	907	882
Br	3783	3478	3511	^b	3703	3738	3685
I	8926	6997	7115	^b	7383	7504	7603
Ne ⁺	761	760	760	815	812	813	780
Ar ⁺	1419	1397	1401	1473	1451	1455	1432
Kr ⁺	5703	5208	5261	^b	5364	5417	5370
Xe ⁺	12957	9988	10156	^b	10232	10404	10537
Rn ⁺	25547	25546	25949	^b	26287	26729	30895
OH	132	132	132	153	152	152	139
SH	359	355	356	388	382	383	377
SeH	1774	1640	1658	^b	1746	1761	1764
TeH	4269	3432	3485	^b	3605	3660	3816
HF ⁺	283	283	283	312	311	311	293
HCl ⁺	635	626	628	662	654	655	648
HBr ⁺	2771	2553	2578	^b	2634	2659	2653
HI ⁺	6261	4998	5074	^b	5118	5196	5400

^a Experimental results are from Refs. 138 and 139.

^b Convergence problems encountered when using the BP Hamiltonian.

similar results for Ag and Au but are somewhat less accurate for Cu with $\sim 6\%$ error. The IP-SR-ADC results show much greater spread, changing significantly (by as much as 1940 cm^{-1}) from IP-SR-ADC(2) to IP-SR-ADC(2)-X.

Overall, our calculations highlight the importance of multireference effects for simulating the ZFS in excited 2D term of Cu, Ag, and Au. These findings can be confirmed with the analysis of CASCI states in the MR-ADC calculations, which reveals that the multireference nature of 2D ex-

cited states increases in the order $\text{Au} > \text{Ag} > \text{Cu}$. Consistent with this analysis, the Cu atom shows the largest difference in $\%$ errors between the SR- and MR-ADC approximations.

4.3 Photoelectron spectra of cadmium halides

In addition to charged excitation energies, the EA/IP-ADC methods provide straightforward access to transition probabilities that can be used

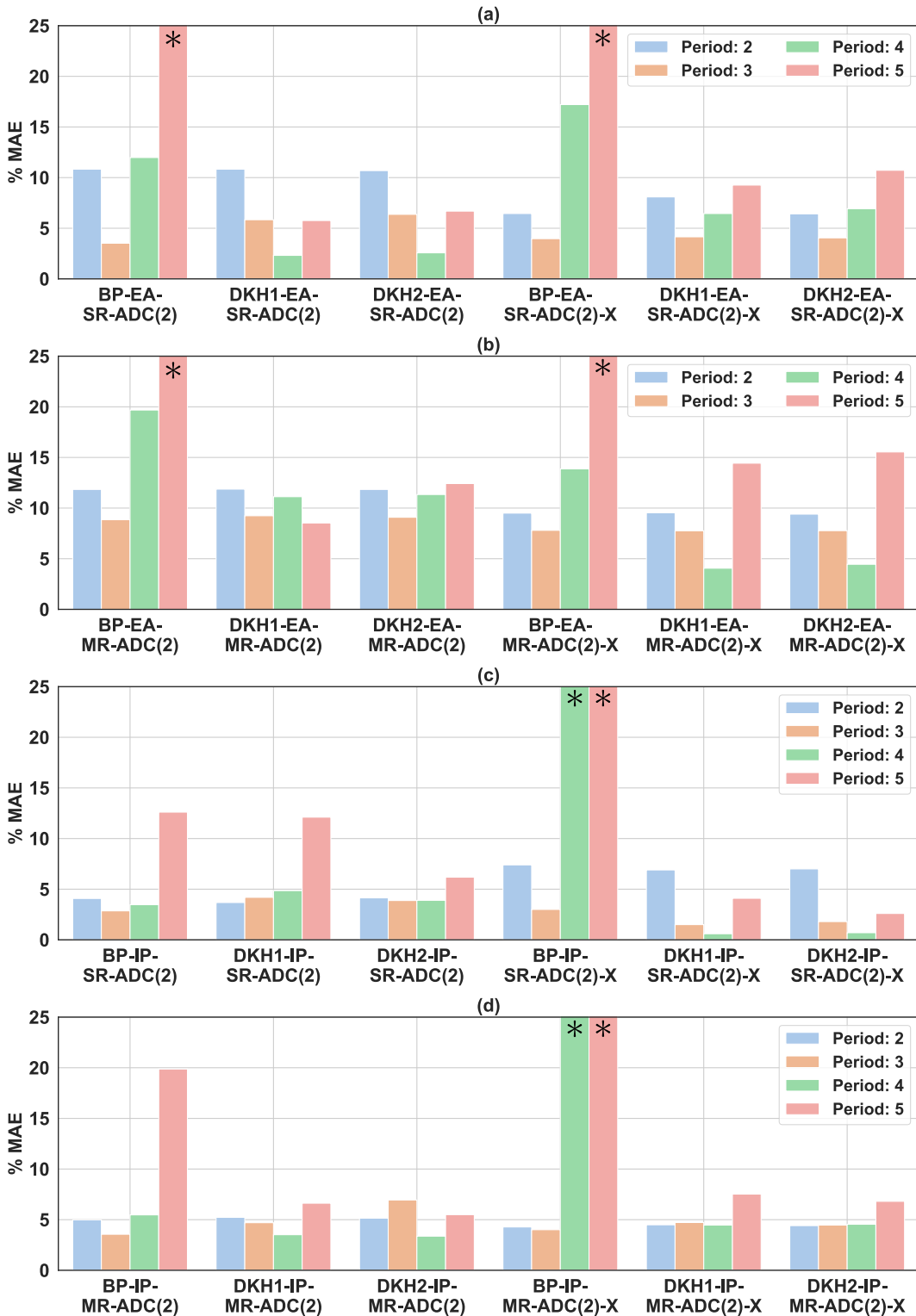


Figure 4: Percent mean absolute errors (% MAE) in the zero-field splitting of main group atoms and diatomics calculated using the two-component EA/IP-ADC methods for the different rows of periodic table relative to the experimental measurements. Bars that exceed the scale are indicated with asterisks. See Tables 2 to 5 for the data on individual systems.

to simulate photoelectron spectra. Here, we use our two-component EA/IP-ADC implementation to compute the photoelectron spectra of linear cadmium halides (CdX_2 , $\text{X} = \text{Cl}, \text{Br}, \text{I}$). Each molecule has a singlet ground state with

the $(\sigma_g)^2(\sigma_u)^2(\pi_u)^4(\pi_g)^4$ electronic configuration in the order of increasing orbital energy. Ionizing the doubly-degenerate π_g and π_u orbitals localized on the halogen atoms gives rise to four electronic states: ${}^2\Pi_{\frac{3}{2}g}$, ${}^2\Pi_{\frac{1}{2}g}$, ${}^2\Pi_{\frac{3}{2}u}$, and ${}^2\Pi_{\frac{1}{2}u}$. The energy

Table 6: Mean absolute errors (cm^{-1}) in the zero-field splitting of main group atoms and diatomics calculated using the two-component EA/IP-ADC methods for periods 2 to 5 of the periodic table relative to the experimental measurements. See Tables 2 to 5 for the data on individual systems.

Method	Period 2	Period 3	Period 4	Period 5
BP-EA-SR-ADC(2)	1.1	1.2	93.4	^a
BP-EA-SR-ADC(2)-X	0.5	2.9	121.5	^a
BP-EA-MR-ADC(2)	1.2	3.6	114.9	^a
BP-EA-MR-ADC(2)-X	1.2	3.6	101.2	^a
DKH1-EA-SR-ADC(2)	1.1	2.7	12.0	111.7
DKH1-EA-SR-ADC(2)-X	0.8	2.8	35.5	169.8
DKH1-EA-MR-ADC(2)	1.3	3.9	33.7	178.8
DKH1-EA-MR-ADC(2)-X	1.3	3.7	19.6	198.4
DKH2-EA-SR-ADC(2)	1.2	3.8	15.7	132.0
DKH2-EA-SR-ADC(2)-X	0.5	2.8	39.4	192.3
DKH2-EA-MR-ADC(2)	1.2	3.8	37.4	209.0
DKH2-EA-MR-ADC(2)-X	1.2	3.7	22.9	220.2
BP-IP-SR-ADC(2)	14.5	19.3	139.8	1264.3
BP-IP-SR-ADC(2)-X	25.8	25.3	^a	^a
BP-IP-MR-ADC(2)	16.6	20.1	234.7	1469.3
BP-IP-MR-ADC(2)-X	14.2	21.3	^a	^a
DKH1-IP-SR-ADC(2)	13.0	31.0	148.3	485.3
DKH1-IP-SR-ADC(2)-X	24.0	13.0	15.3	254.5
DKH1-IP-MR-ADC(2)	17.7	30.2	76.5	409.5
DKH1-IP-MR-ADC(2)-X	15.2	27.6	97.2	452.8
DKH2-IP-SR-ADC(2)	14.9	28.3	116.1	381.4
DKH2-IP-SR-ADC(2)-X	24.5	15.3	27.3	148.1
DKH2-IP-MR-ADC(2)	17.3	63.8	82.1	333.1
DKH2-IP-MR-ADC(2)-X	14.9	25.0	110.6	407.6

^a Convergence problems encountered when using the BP Hamiltonian.

Table 7: Zero-field splitting (cm^{-1}) in the ground 2D term of Sc, Y and La atoms computed using the two-component EA-ADC methods. For comparison, we also include data from DKH2-QDNEVPT2⁷⁹ and X2C-MRCISD.⁷¹ All calculations employed the X2C-TZVPall-2c basis set. Shown in parentheses are the % errors with respect to experimental results.¹³⁹⁻¹⁴¹

Method	Sc	Y	La
DKH2-QDNEVPT2 ⁷⁹	141 (16.3)	428 (19.2)	897 (14.9)
X2C-MRCISD ⁷¹	186 (10.2)	524 (1.1)	936 (11.2)
BP-EA-SR-ADC(2)	108 (35.5)	381 (28.2)	^a
DKH1-EA-SR-ADC(2)	110 (34.7)	392 (26.1)	987 (6.2)
DKH2-EA-SR-ADC(2)	110 (34.8)	391 (26.3)	987 (6.2)
BP-EA-SR-ADC(2)-X	131 (22.0)	450 (15.1)	^a
DKH1-EA-SR-ADC(2)-X	132 (21.3)	457 (13.7)	1094 (3.9)
DKH2-EA-SR-ADC(2)-X	132 (21.4)	457 (13.8)	1095 (4.0)
BP-EA-MR-ADC(2)	109 (35.3)	385 (27.4)	973 (7.6)
DKH1-EA-MR-ADC(2)	110 (34.6)	396 (25.3)	1002 (4.9)
DKH2-EA-MR-ADC(2)	110 (34.6)	395 (25.5)	1002(4.9)
BP-EA-MR-ADC(2)-X	132 (21.3)	454 (14.3)	^a
DKH1-EA-MR-ADC(2)-X	133 (20.7)	461 (12.9)	1089 (3.4)
DKH2-EA-MR-ADC(2)-X	133 (20.7)	461 (13.0)	1090 (3.5)
Experiment	168	530	1053

^a Convergence problems encountered when using the BP Hamiltonian.

spacing and relative order of these states in CdX_2^+ depends on the strength of spin-orbit coupling that increases from $X = \text{Cl}$ to $X = \text{I}$.

Figure 5 compares the experimental photoelec-

tron spectra^{133,134} of CdX_2 ($X = \text{Cl}, \text{Br}, \text{I}$) with the results of DKH2-IP-MR/SR-ADC(2) and DKH2-IP-MR/SR-ADC(2)-X calculations. The simulated spectra were uniformly shifted to align their lowest-

Table 8: Zero-field splitting (cm^{-1}) in the excited 2D term of Cu, Ag, and Au atoms computed using the two-component IP-ADC methods. All calculations employed the X2C-TZVPall-2c basis set. Shown in parentheses are the % errors with respect to experimental results. ¹⁴²⁻¹⁴⁴

Method	Cu	Ag	Au
BP-IP-SR-ADC(2)	1787 (12.5)	4071 (9.0)	11547 (5.9)
DKH1-IP-SR-ADC(2)	1785 (12.6)	4027 (9.9)	11105 (9.5)
DKH2-IP-SR-ADC(2)	1786 (12.6)	4034 (9.8)	11168 (9.0)
BP-IP-SR-ADC(2)-X	2181 (6.8)	4727 (5.7)	^a
DKH1-IP-SR-ADC(2)-X	2177 (6.6)	4659 (4.2)	13030 (6.2)
DKH2-IP-SR-ADC(2)-X	2178 (6.6)	4668 (4.4)	13108 (6.8)
BP-IP-MR-ADC(2)	1927 (5.7)	4291 (4.0)	12109 (1.3)
DKH1-IP-MR-ADC(2)	1925 (5.8)	4245 (5.1)	11602 (5.5)
DKH2-IP-MR-ADC(2)	1926 (5.7)	4251 (4.9)	11666 (4.9)
BP-IP-MR-ADC(2)-X	1984 (2.9)	4344 (2.9)	^a
DKH1-IP-MR-ADC(2)-X	2019 (1.1)	4292 (4.0)	11490 (6.4)
DKH2-IP-MR-ADC(2)-X	2021 (1.1)	4299 (3.9)	11547 (5.9)
Experiment	2043	4472	12274

^a Convergence problems encountered when using the BP Hamiltonian.

Table 9: Relative energies (ΔE , eV) of states in the CdX_2^+ molecules ($X = \text{Cl}, \text{Br}, \text{I}$) calculated using DKH2-IP-ADC methods in comparison to experimental data. ^{133,134} For the $^2\Pi_{\frac{3}{2}g}$ state, vertical ionization energy (VIE, eV) is reported. All calculations employed the X2C-QZVPall basis set.

Molecule	Property	SR-ADC(2)	SR-ADC(2)-X	MR-ADC(2)	MR-ADC(2)-X	Experiment
CdCl_2^+	VIE ($^2\Pi_{\frac{3}{2}g}$)	11.00	10.89	12.23	11.85	11.49
	$\Delta E(^2\Pi_{\frac{1}{2}g} - ^2\Pi_{\frac{3}{2}g})$	0.08	0.09	0.09	0.09	$\lesssim 0.1$
	$\Delta E(^2\Pi_{\frac{3}{2}u} - ^2\Pi_{\frac{1}{2}g})$	0.37	0.34	0.39	0.43	0.40
	$\Delta E(^2\Pi_{\frac{1}{2}u} - ^2\Pi_{\frac{3}{2}u})$	0.07	0.08	0.08	0.08	$\lesssim 0.1$
	$\Delta E(^2\Sigma_u - ^2\Pi_{\frac{1}{2}u})$	0.68	0.65	0.59	0.67	0.49
CdBr_2^+	VIE ($^2\Pi_{\frac{3}{2}g}$)	10.27	10.12	11.28	10.99	10.58
	$\Delta E(^2\Pi_{\frac{1}{2}g} - ^2\Pi_{\frac{3}{2}g})$	0.30	0.32	0.31	0.31	0.31
	$\Delta E(^2\Pi_{\frac{3}{2}u} - ^2\Pi_{\frac{1}{2}g})$	0.14	0.10	0.15	0.18	0.15
	$\Delta E(^2\Pi_{\frac{1}{2}u} - ^2\Pi_{\frac{3}{2}u})$	0.24	0.25	0.24	0.24	0.21
	$\Delta E(^2\Sigma_u - ^2\Pi_{\frac{1}{2}u})$	0.70	0.70	0.64	0.69	0.60
CdI_2^+	VIE ($^2\Pi_{\frac{3}{2}g}$)	9.49	9.31	10.45	10.22	9.55
	$\Delta E(^2\Pi_{\frac{3}{2}u} - ^2\Pi_{\frac{3}{2}g})$	0.39	0.37	0.40	0.43	0.43
	$\Delta E(^2\Pi_{\frac{1}{2}g} - ^2\Pi_{\frac{3}{2}u})$	0.18	0.23	0.19	0.16	0.20
	$\Delta E(^2\Pi_{\frac{1}{2}u} - ^2\Pi_{\frac{1}{2}g})$	0.16	0.13	0.13	0.18	0.17
	$\Delta E(^2\Sigma_u - ^2\Pi_{\frac{3}{2}u})$	0.90	0.94	0.92	0.93	0.86
	$\Delta E(^2\Sigma_g - ^2\Sigma_u)$	1.01	0.96	0.90	0.91	1.05

energy peak with the corresponding signal in the experimental data. Apart from the shift, all four levels of theory predict the same order of states and qualitatively reproduce the peak structure in experimental spectra. For CdCl_2 , four peaks are observed in the simulated and experimental photoelectron spectra. The first two peaks correspond to two pairs of states ($^2\Pi_{\frac{3}{2}g} - ^2\Pi_{\frac{1}{2}g}$ and $^2\Pi_{\frac{3}{2}u} - ^2\Pi_{\frac{1}{2}u}$) with each pair split by $\lesssim 0.1$ eV due to weak spin-orbit coupling.

Stronger zero-field splitting in CdBr_2 and CdI_2

merges the signals from $^2\Pi_g$ and $^2\Pi_u$ states into a broad band and reorders $^2\Pi_{\frac{1}{2}g}$ and $^2\Pi_{\frac{3}{2}u}$ in cadmium iodide. The shape of this band in experimental spectra is qualitatively reproduced by all two-component IP-ADC methods, suggesting that multireference effects are not important for the low-energy ionized states of cadmium halides. The IP-ADC calculations are also in a good agreement with the photoelectron spectra from two-component self-consistent GW reported recently by Abraham et al. ¹⁴⁵

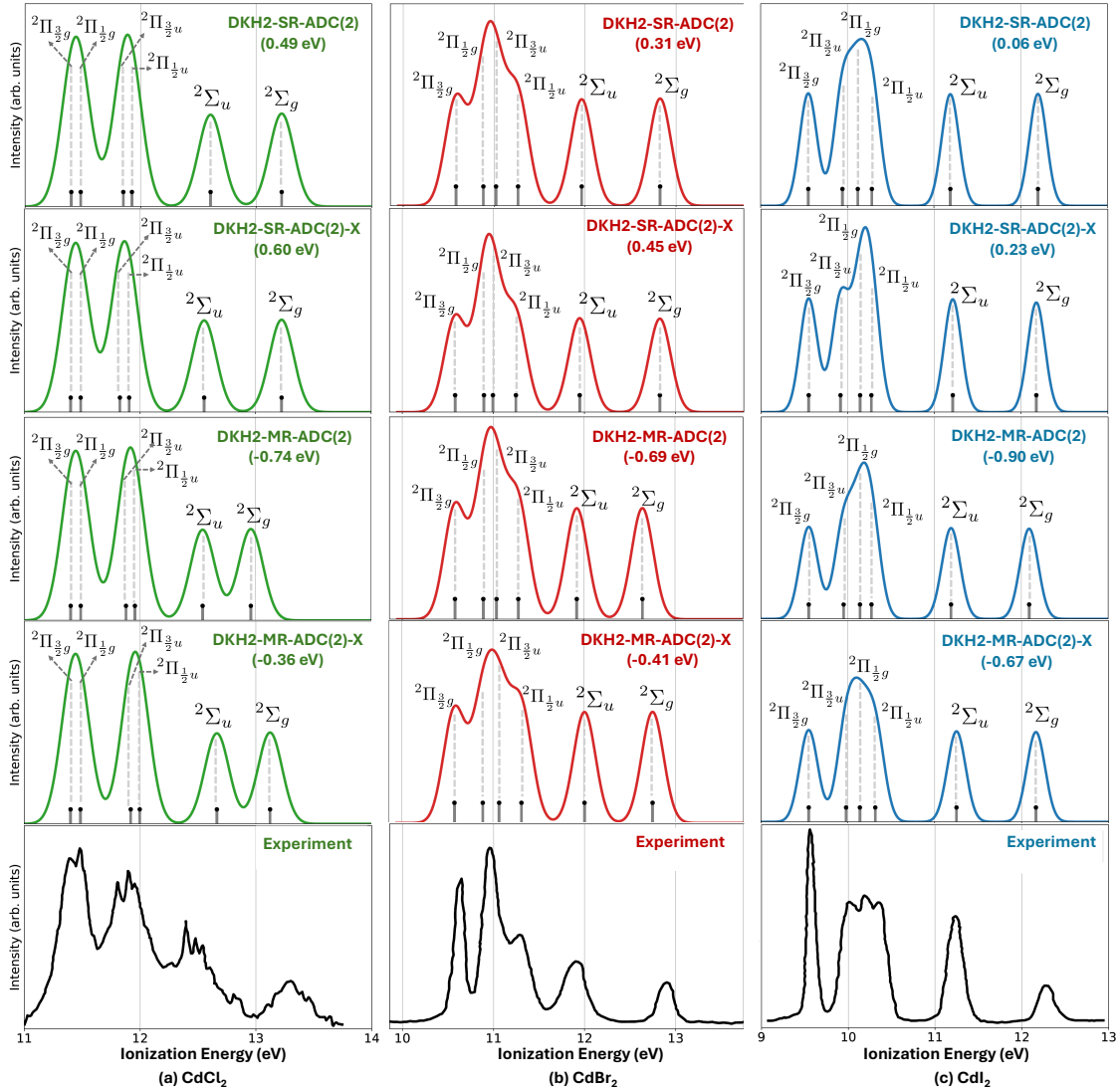


Figure 5: Photoelectron spectra of cadmium dihalides (CdX_2 , $X = \text{Cl}, \text{Br}, \text{and I}$) simulated using two-component IP-SR-ADC and IP-MR-ADC methods with the DKH2 spin-orbit Hamiltonian. Calculated spectra were shifted to align them with the experimental spectra for the first peak. The shift value is indicated in parentheses for each spectrum. Experimental spectra were digitized¹³² and reprinted from Refs. 133 and 134 with permission from Elsevier and Wiley Materials. Copyright 1983 and 2011.

Table 9 reports the relative energies of CdX_2^+ ($X = \text{Cl}, \text{Br}, \text{I}$) states in the experimental and simulated spectra. All two-component ADC methods predict the relative spacing between the first four states within $\lesssim 0.06$ eV of experimental measurements. The ${}^2\Pi_{1/2u} - {}^2\Sigma_u$ energy separations are consistently overestimated in all ADC calculations by up to 0.2 eV. The most significant deviations from experimental data are observed for the ${}^2\Sigma_u - {}^2\Sigma_g$ relative energies, which are systematically underestimated by 0.1 to 0.4 eV with errors increasing from $X = \text{I}$ to $X = \text{Cl}$. Due to the dissociative nature of ${}^2\Sigma_u$ and ${}^2\Sigma_g$ states,¹³⁴ accurately simulating their signals in photoelectron spectra may require considering the effects of nuclear dynamics,

which are missing in our calculations.

4.4 Photoelectron spectra of methyl iodide along bond dissociation

Finally, we showcase the multireference capabilities of our two-component EA/IP-ADC implementation by simulating the photoelectron spectrum of methyl iodide (CH_3I) along the C-I bond dissociation. Due to its small size, dissociative low-lying excited states, and strong spin-orbit coupling, CH_3I has become a prototype for testing new experimental and theoretical techniques aimed at understanding the electronic structure and coupled electron-nuclear dynamics at atto- and femtosecond times scales.^{146–167} Most studies have fo-

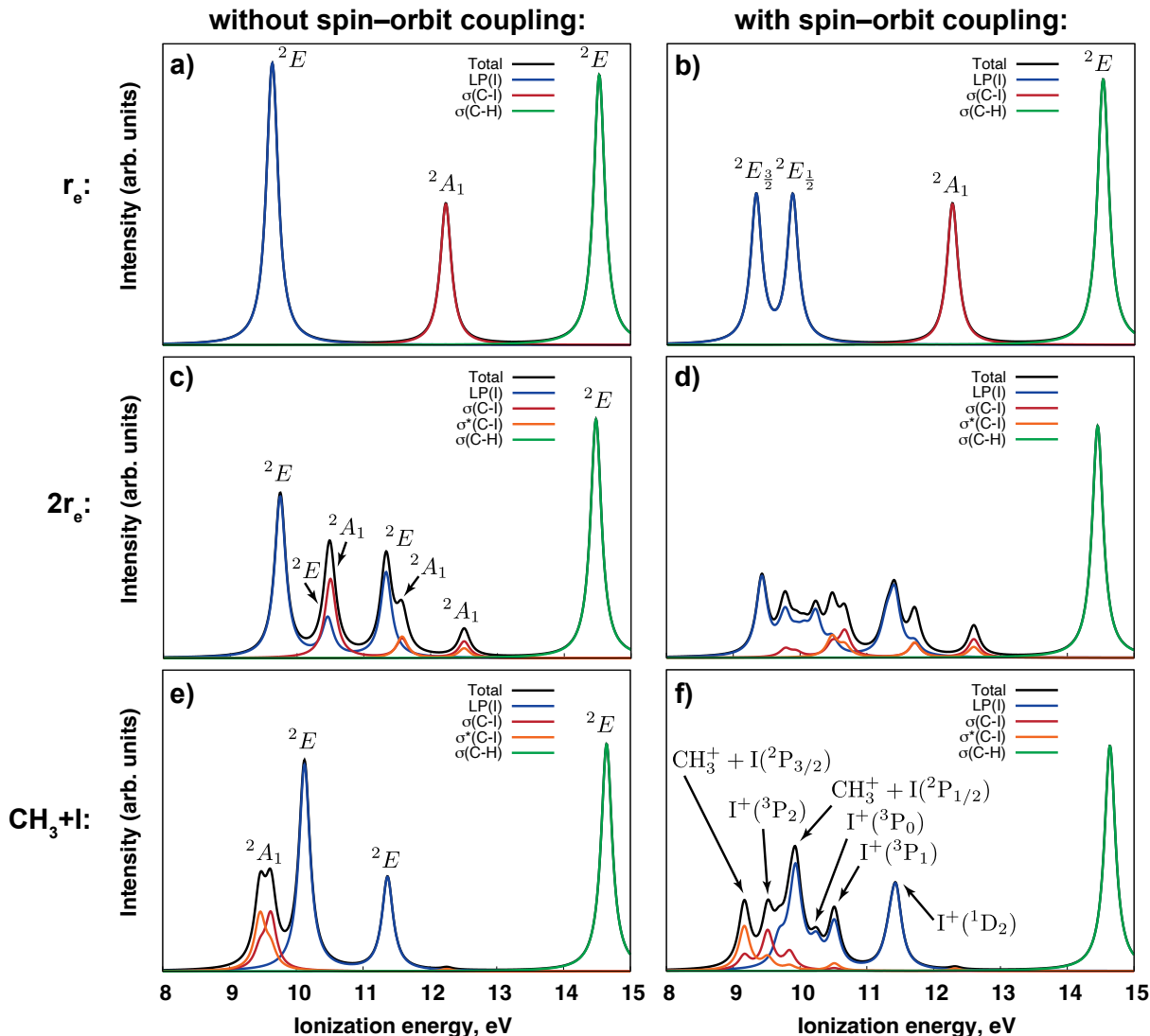


Figure 6: Photoelectron spectra of methyl iodide (CH_3I) computed using the DKH2-IP-MR-ADC method at the equilibrium (r_e , a and b), stretched ($2r_e$, c and d), and dissociated (CH_3+I , e and f) geometries. Spectra were calculated with (b, d, f) and without (a, c, e) spin-orbit coupling effects. Each plot shows photoelectron intensity contributions from the iodine lone-pair (LP(I)), C-I σ -bonding ($\sigma(\text{C-I})$), C-I σ -antibonding ($\sigma^*(\text{C-I})$), and C-H σ -bonding ($\sigma(\text{C-H})$) orbitals.

cused on investigating the CH_3I photodissociation dynamics following an excitation into the first absorption band at 220 – 350 nm (so-called *A*-band), which promotes electrons from the iodine lone pairs into the C-I antibonding orbital ($n \rightarrow \sigma^*$). In particular, time-resolved (pump-probe) photoelectron spectroscopy provided valuable insights about the CH_3I photodissociation mechanism by measuring electron binding energies as a function of time.^{148,150,153,158,161,164,166,167} Comparing the results of these measurements with accurate theoretical calculations provides opportunities to obtain deeper insights about the interplay of spin-orbit coupling, strong electron correlation, and nonadiabatic relaxation in photodissociation dynamics.

Here, we investigate the effect of spin-orbit cou-

pling on the photoelectron spectra of CH_3I computed at equilibrium (r_e), stretched ($2r_e$), and completely dissociated (CH_3+I) geometries. In the stretched structure, the C-I bond was elongated by a factor of two relative to its equilibrium value but the geometry of CH_3 fragment was kept frozen. For the dissociated structure, the iodine atom was placed $\sim 6.7 \text{ \AA}$ away from the carbon atom and the geometry of CH_3 moiety was fully optimized.

Figure 6 shows the r_e , $2r_e$, and CH_3+I photoelectron spectra simulated using DKH2-IP-MR-ADC(2)-X with and without spin-orbit coupling effects. The r_e photoelectron spectrum simulated without spin-orbit coupling (Figure 6a) exhibits only three peaks corresponding to the electron detachment from the iodine lone pairs (1^2E , LP(I)),

the C–I σ -bonding orbital (1^2A_1 , $\sigma(\text{C–I})$), and the C–H bonding orbitals of CH_3 fragment (2^2E , $\sigma(\text{C–H})$). Including spin–orbit coupling splits the 1^2E transition into the $1^2E_{3/2}$ and $1^2E_{1/2}$ components with the zero-field splitting (ZFS) of 0.55 eV at the DKH2-IP-MR-ADC(2)-X/X2C-TZVPall level of theory (Figure 6b). The computed ($1^2E_{3/2}$; $1^2E_{1/2}$) vertical ionization energies (9.33; 9.88 eV) are in a good agreement with the experimental binding energies (9.54; 10.17 eV) reported by Loch et al.¹⁶⁰ For the two higher-lying states (1^2A_1 , 2^2E), the experimental photoelectron spectrum shows broad bands at 12.1–13.1 and 14–15.6 eV with maxima at 12.6 and 14.8 eV. These measurements agree well with the calculated (1^2A_1 ; $2^2E_{3/2}$; $2^2E_{1/2}$) vertical ionization energies of (12.27; 14.52; 14.53) eV where the $2^2E_{3/2} - 2^2E_{1/2}$ splitting ($\sim 90 \text{ cm}^{-1} \approx 0.01 \text{ eV}$) is due to a very weak spin–orbit coupling in the ionized CH_3 group. It is important to point out that the 2^2E states correspond to ionizing the non-active $8e$ molecular orbitals. Since DKH2-IP-MR-ADC(2)-X incorporates the full spectrum of single and double excitations (Section 2.2), the 2^2E transitions can be included without expanding the active space.

Stretching the C–I bond by a factor of two ($2r_e$) results in a more complicated photoelectron spectrum. Comparing the r_e and $2r_e$ spectra without spin–orbit coupling effects (Figures 6a and 6c), large red shift and lowering of intensity are observed for the lowest-energy 2^2A_1 peak due to the weakening of $\sigma(\text{C–I})$. In addition, two new 2^2A_1 signals appear with smaller intensities. As shown in Figure 6c, these features correspond to the ionization of C–I antibonding orbital ($\sigma^*(\text{C–I})$) that is significantly populated at this stretched geometry. Since the 2^2E state is localized on iodine lone pairs (LP(I)), its energy increases by only 0.13 eV. However, a significant fraction of 2^2E intensity is transferred into the higher-lying 2^2E states that appear 0.7 and 1.6 eV higher in energy. Incorporating spin–orbit coupling results in the zero-field splitting of 2^2E states and allows them to interact with 2^2A_1 , which further complicates the spectrum (Figure 6d). Although we cannot assign symmetries for each peak in Figure 6d, we note that the energy separations and orbital character of states in our DKH2-IP-MR-ADC(2)-X calculations with and without spin–orbit coupling are in a good agreement with the results of a multireference configuration interaction study by Marggi Poulain and co-workers.¹⁶³ Interestingly, incorporating

spin–orbit coupling results in a much stronger overlap of photoelectron signals from $\sigma(\text{C–I})$ and $\sigma^*(\text{C–I})$, which indicates that this effect facilitates bond breaking at this geometry.

Finally, we consider the photoelectron spectra computed for the fully dissociated CH_3+I structure with a relaxed (planar) CH_3 fragment. Without spin–orbit effects (Figure 6e), the CH_3+I spectrum exhibits fewer features compared to that at the $2r_e$ geometry (Figure 6c). Relaxing the CH_3 geometry red shifts the two lowest-energy 2^2A_1 transitions corresponding to the ionization of CH_3 radical and I atom. As a result of complete C–I bond dissociation, the first 2^2E transition blue shifts by $\sim 0.37 \text{ eV}$, gaining intensity relative to the $2r_e$ spectrum. Incorporating spin–orbit coupling (Figure 6f) significantly perturbs the spectrum, splitting the peaks and allowing the resulting states interact. As discussed in Ref. 163, the ionized states of CH_3+I can be assigned to the $\text{CH}_3 + \text{I}^+$ and $\text{CH}_3^+ + \text{I}$ dissociation limits with I or I^+ in their ground or excited electronic states. Due to spatial symmetry breaking in the reference CASSCF wavefunction, the degeneracy of some $\text{CH}_3 + \text{I}^+$ and $\text{CH}_3^+ + \text{I}$ states in our calculations is lifted by $\sim 0.05 \text{ eV}$ on average with a maximum of $\sim 0.15 \text{ eV}$. Despite this, for the features with significant intensity tentative assignments can be made as follows: $\text{CH}_3^+ + \text{I}(^2P_{3/2})$ [9.2 eV], $\text{CH}_3 + \text{I}^+(^3P_2)$ [9.5 eV], $\text{CH}_3^+ + \text{I}(^2P_{1/2})$ [9.9 eV], $\text{CH}_3 + \text{I}^+(^3P_0)$ [10.3 eV], $\text{CH}_3 + \text{I}^+(^3P_1)$ [10.5 eV], and $\text{CH}_3 + \text{I}^+(^1D_2)$ [11.4 eV]. For the $\text{CH}_3^+ + \text{I}$ ionization channel, these results are in a good agreement with the data from femtosecond pump-probe experiments by de Nalda et al.¹⁵⁶ that reported the first ionization energy of $\sim 9.3 \text{ eV}$ and the $\text{I}(^2P_{3/2}) - \text{I}(^2P_{1/2})$ zero-field splitting of $\sim 0.8 \text{ eV}$. In the $\text{CH}_3 + \text{I}^+$ channel, the energy separations of I^+ levels ($^3P_0 - ^3P_2$, $^3P_1 - ^3P_0$, $^1D_2 - ^3P_1$) computed using DKH2-IP-MR-ADC(2)-X (0.8, 0.2, 0.9 eV) agree well with the data from atomic spectroscopy (0.8, 0.1, 0.8 eV).¹³⁹

5 Conclusion

We presented a two-component formulation of algebraic diagrammatic construction theory that enables simulating charged electronic states and photoelectron spectra with a computationally efficient treatment of electron correlation (both static and dynamic) and spin–orbit coupling. Starting with either a restricted Hartree–Fock or a complete ac-

tive space self-consistent field reference wavefunction, our implementation allows to perform single-reference (SR-) or multireference (SR- and MR-) ADC calculations incorporating dynamic correlation and spin-orbit coupling up to the second order in perturbation theory. The relativistic effects are described using three flavors of two-component spin-orbit Hamiltonians, namely: Breit-Pauli, first-order Douglas-Kroll-Hess, and second-order Douglas-Kroll-Hess.

We benchmarked the accuracy of two-component SR- and MR-ADC methods for simulating zero-field splitting and photoelectron spectra of atoms and small molecules. When multireference effects are not important, such as in main group atoms and diatomics, the SR-ADC methods are competitive in accuracy to the MR-ADC approximations, often showing better agreement with experimental results. However, as we demonstrated in our studies of d^9 transition metal atoms and the methyl iodide molecule, the MR-ADC methods are more reliable in excited states and can correctly describe photoelectron spectra in non-equilibrium regions of potential energy surfaces that can be important for interpreting the results of time-resolved experiments.

Overall, our benchmark results demonstrate that the two-component ADC methods developed in this work are promising techniques for efficient and accurate simulations of spin-orbit coupling in charged electronic states. To make them practical, several developments are still necessary, such as efficient computer implementation, enabling calculations for degenerate or state-averaged reference states, and extensions to neutral excitations. The two-component ADC methods are also attractive for simulating how matter interacts with high-energy light, as was demonstrated in a recent study of time-resolved X-ray photoelectron spectra along iron pentacarbonyl photodissociation.⁸⁷ Pushing these frontiers holds promise for improving our understanding of relativistic effects and electron correlation in increasingly complicated molecular systems.

6 Appendix: Deriving Amplitude Equations for the Internal Single Excitations

As discussed in Section 2.3, incorporating H_{SO} (Eq. (24)) in the perturbation term V of MR-ADC

effective Hamiltonian (Eqs. (16) and (17)) results in new contributions to \mathbf{M}_{\pm} (Eqs. (9) and (12)) starting at the first order in perturbation theory. Since H_{SO} contains terms with all active indices (i.e., spin-orbit coupling in active orbitals), diagonal blocks of $\mathbf{M}_{\pm}^{(k)}$ ($k \geq 1$) with the excitation operators $h_{\pm\mu}^{(l)\dagger}$ and $h_{\pm\nu}^{(l)}$ belonging to the same class will get modified. As an example, we consider the diagonal sectors of $\mathbf{M}_{+}^{(k)}$ in two-component EA-MR-ADC that can be written as:

$$\begin{aligned} M_{+\mu\nu}^{(k)} &= \sum_{lm}^{l+m=k} \langle \Psi_0 | [h_{+\mu}^{(l)}, [\tilde{H}^{(m)}, h_{+\nu}^{(l)\dagger}]]_+ | \Psi_0 \rangle \\ &= \sum_{lm}^{l+m=k} \left(\langle \Psi_0 | h_{+\mu}^{(l)} \tilde{H}^{(m)} h_{+\nu}^{(l)\dagger} | \Psi_0 \rangle \right. \\ &\quad \left. - \langle \Psi_0 | h_{+\mu}^{(l)} h_{+\nu}^{(l)\dagger} \tilde{H}^{(m)} | \Psi_0 \rangle \right) \end{aligned} \quad (30)$$

We also write down an expression for the same diagonal block of $\mathbf{M}_{\pm}^{(k)\dagger}$:

$$\begin{aligned} M_{+\mu\nu}^{(k)\dagger} &= \sum_{lm}^{l+m=k} \langle \Psi_0 | [h_{+\nu}^{(l)}, [\tilde{H}^{(m)}, h_{+\mu}^{(l)\dagger}]]_+ | \Psi_0 \rangle^\dagger \\ &= \sum_{lm}^{l+m=k} \left(\langle \Psi_0 | h_{+\mu}^{(l)\dagger} \tilde{H}^{(m)} h_{+\nu}^{(l)} | \Psi_0 \rangle \right. \\ &\quad \left. - \langle \Psi_0 | \tilde{H}^{(m)} h_{+\mu}^{(l)\dagger} h_{+\nu}^{(l)} | \Psi_0 \rangle \right) \end{aligned} \quad (31)$$

where we used the fact that $\tilde{H}^{(m)}$ is Hermitian at any order m . Comparing Eqs. (30) and (31), we note that for the effective Hamiltonian matrix to be Hermitian ($M_{+\mu\nu}^{(k)} = M_{+\mu\nu}^{(k)\dagger}$) their last terms should be zero or equal to each other. Since $h_{+\mu}^{(l)}$ and $h_{+\nu}^{(l)\dagger}$ are from the same class, these contributions correspond to the projections of $\tilde{H}^{(m)}$ by excitations inside active space (so-called internal excitations). Due to the all-active contributions from H_{SO} , the last two terms in the Eqs. (30) and (31) are generally not the same, unless the effective Hamiltonian is parameterized to prevent that.

To ensure that $\mathbf{M}_{\pm}^{(k)}$ is rigorously Hermitian up to $k = 2$, we incorporate a new class of first-order internal excitations in the correlation operator T :

$$T^{(1)} \leftarrow \sum_{x>y} t_x^{y(1)} a_y^\dagger a_x \quad (32)$$

which ensure that the last two terms of Eqs. (30) and (31) (and similar terms in IP-MR-ADC) are equal to each other.⁸⁴ The $t_x^{y(1)}$ ($x > y$) ampli-

tudes are determined by solving a system of linear equations:

$$\langle \Psi_0 | a_x^\dagger a_y \tilde{H}^{(1)} | \Psi_0 \rangle - \langle \Psi_0 | a_y^\dagger a_x \tilde{H}^{(1)} | \Psi_0 \rangle^* = 0 \quad (33)$$

Since $t_x^{y(1)}$ are complex-valued, Eq. (33) need be solved for $\text{Re}(t_x^{y(1)})$ and $\text{Im}(t_x^{y(1)})$ separately. Each system of equations can be written in a tensor form:

$$\mathbf{K}_{\text{Re}} \mathbf{T}_{\text{Re}}^{(1)} = -\mathbf{V}_{\text{Re}} \quad (34)$$

$$\mathbf{K}_{\text{Im}} \mathbf{T}_{\text{Im}}^{(1)} = -\mathbf{V}_{\text{Im}} \quad (35)$$

where $\mathbf{T}_{\text{Re}}^{(1)}$ and $\mathbf{T}_{\text{Im}}^{(1)}$ contain the real and imaginary parts of $t_x^{y(1)}$ ($x > y$), respectively. The elements of \mathbf{K}_{Re} , \mathbf{K}_{Im} , \mathbf{V}_{Re} , and \mathbf{V}_{Im} are defined as:

$$K_{xy,wz}^{\text{Re}} = \langle \Psi_0 | (a_x^\dagger a_y - a_y^\dagger a_x) [H^{(0)}, a_z^\dagger a_w - a_w^\dagger a_z] | \Psi_0 \rangle \quad (36)$$

$$K_{xy,wz}^{\text{Im}} = \langle \Psi_0 | (a_x^\dagger a_y + a_y^\dagger a_x) [H^{(0)}, a_z^\dagger a_w + a_w^\dagger a_z] | \Psi_0 \rangle \quad (37)$$

$$V_{xy}^{\text{Re}} = \text{Re}(\langle \Psi_0 | (a_x^\dagger a_y - a_y^\dagger a_x) V_{2c} | \Psi_0 \rangle) \quad (38)$$

$$V_{xy}^{\text{Im}} = \text{Im}(\langle \Psi_0 | (a_x^\dagger a_y + a_y^\dagger a_x) V_{2c} | \Psi_0 \rangle) \quad (39)$$

where $H^{(0)}$ is the Dyall zeroth-order Hamiltonian and V_{2c} is the perturbation operator defined in Eq. (29).

To solve Eqs. (34) and (35), we first diagonalize the real-valued and Hermitian \mathbf{K}_{Re} and \mathbf{K}_{Im} matrices:

$$\mathbf{K}_{\text{Re}} \mathbf{Z}_{\text{Re}} = \mathbf{S}_{\text{Re}} \mathbf{Z}_{\text{Re}} \boldsymbol{\epsilon}_{\text{Re}} \quad (40)$$

$$\mathbf{K}_{\text{Im}} \mathbf{Z}_{\text{Im}} = \mathbf{S}_{\text{Im}} \mathbf{Z}_{\text{Im}} \boldsymbol{\epsilon}_{\text{Im}} \quad (41)$$

where \mathbf{Z}_{Re} and \mathbf{Z}_{Im} denote the eigenvectors of corresponding generalized eigenvalue problems and \mathbf{S}_{Re} and \mathbf{S}_{Im} are the overlap matrices:

$$S_{xy,wz}^{\text{Re}} = \langle \Psi_0 | (a_x^\dagger a_y - a_y^\dagger a_x) (a_z^\dagger a_w - a_w^\dagger a_z) | \Psi_0 \rangle \quad (42)$$

$$S_{xy,wz}^{\text{Im}} = \langle \Psi_0 | (a_x^\dagger a_y + a_y^\dagger a_x) (a_z^\dagger a_w + a_w^\dagger a_z) | \Psi_0 \rangle \quad (43)$$

The contributions to internal amplitudes can then be obtained as follows:

$$\mathbf{T}_{\text{Re}}^{(1)} = -\mathbf{S}_{\text{Re}}^{-1/2} \tilde{\mathbf{Z}}_{\text{Re}} \boldsymbol{\epsilon}_{\text{Re}}^{-1} \tilde{\mathbf{Z}}_{\text{Re}}^\dagger \mathbf{S}_{\text{Re}}^{-1/2} \mathbf{V}_{\text{Re}} \quad (44)$$

$$\mathbf{T}_{\text{Im}}^{(1)} = -\mathbf{S}_{\text{Im}}^{-1/2} \tilde{\mathbf{Z}}_{\text{Im}} \boldsymbol{\epsilon}_{\text{Im}}^{-1} \tilde{\mathbf{Z}}_{\text{Im}}^\dagger \mathbf{S}_{\text{Im}}^{-1/2} \mathbf{V}_{\text{Im}} \quad (45)$$

where $\tilde{\mathbf{Z}}_{\text{Re}} = \mathbf{S}_{\text{Re}}^{1/2} \mathbf{Z}_{\text{Re}}$ and $\tilde{\mathbf{Z}}_{\text{Im}} = \mathbf{S}_{\text{Im}}^{1/2} \mathbf{Z}_{\text{Im}}$.

Acknowledgement

This work was supported by the National Science Foundation, under Grant No. CHE-2044648. Computations were performed at the Ohio Supercomputer Center under Project No. PAS1583.¹⁶⁸

Supporting Information Available

Additional computational details, including geometries, reference active spaces, and the selection of CASCI states for each calculation.

References

- (1) Morab, S.; Sundaram, M. M.; Pivrikas, A. Review on Charge Carrier Transport in Inorganic and Organic Semiconductors. *Coatings* **2023**, *Vol. 13*, Page 1657 **2023**, *13*, 1657.
- (2) Sur, S.; Mondal, R.; Thotiyl, M. O. OH-/H+ dual-ion energy assisted electricity effective photoelectrochemical water splitting. *J. Photochem. Photobiol.* **2023**, *16*, 100190.
- (3) Koike, T. Recent progress in photocatalytic reactions involving the excitation of electron-primed catalysts. *J. Photochem. Photobiol.* **2023**, *17*, 100205.
- (4) Umstead, M. E.; Woods, F. J.; Johnson, J. E. A study of the ionization produced by the catalytic combustion of hydrocarbons. *J. Catal.* **1966**, *5*, 293–300.
- (5) Uddin, N.; Zhang, H.; Du, Y.; Jia, G.; Wang, S.; Yin, Z. Structural-phase catalytic redox reactions in energy and environmental applications. *Adv. Mater.* **2020**, *32*, 1905739.
- (6) Steenken, S. Purine bases, nucleosides, and nucleotides: aqueous solution redox chemistry and transformation reactions of their radical cations and e- and OH adducts. *Chem. Rev.* **1989**, *89*, 503–520.
- (7) Yan, M.; Becker, D.; Summerfield, S.; Renke, P.; Sevilla, M. D. Relative abundance and reactivity of primary ion radicals in gamma-irradiated DNA at low temperatures. 2. Single-vs double-stranded DNA. *J. Phys. Chem.* **1992**, *96*, 1983–1989.

- (8) Huels, M. A.; Hahndorf, I.; Illenberger, E.; Sanche, L. Resonant dissociation of DNA bases by subionization electrons. *J. Chem. Phys.* **1998**, *108*, 1309–1312.
- (9) Tonti, D.; Zanoni, R. Measurement Methods — Electronic and Chemical Properties: X-Ray Photoelectron Spectroscopy. *Encycl. Electrochem. Power Sources* **2009**, 673–695.
- (10) Marsh, B. M.; Lamoureux, B. R.; Leone, S. R. Ultrafast time-resolved extreme ultraviolet (XUV) photoelectron spectroscopy of hole transfer in a Zn/n-GaP Schottky junction. *Struct. Dyn.* **2018**, *5*, 54502.
- (11) Perry, C. F.; Jordan, I.; Zhang, P.; Von Conta, A.; Nunes, F. B.; Wörner, H. J. Photoelectron Spectroscopy of Liquid Water with Tunable Extreme-Ultraviolet Radiation: Effects of Electron Scattering. *J. Phys. Chem. Lett.* **2021**, *12*, 2990–2996.
- (12) Zanni, M. T.; Batista, V. S.; Greenblatt, B. J.; Miller, W. H.; Neumark, D. M. Femtosecond photoelectron spectroscopy of the I²⁻ anion. *J. Chem. Phys.* **1999**, *110*, 3748–3755.
- (13) Stolow, A.; Bragg, A. E.; Neumark, D. M. Femtosecond time-resolved photoelectron spectroscopy. *Chem. Rev.* **2004**, *104*, 1719–1757.
- (14) Zhang, C. H.; Thumm, U. Attosecond photoelectron spectroscopy of metal surfaces. *Phys. Rev. Lett.* **2009**, *102*, 123601.
- (15) Jadoun, D.; Kowalewski, M. Time-Resolved Photoelectron Spectroscopy of Conical Intersections with Attosecond Pulse Trains. *J. Phys. Chem. Lett.* **2021**, *12*, 8103–8108.
- (16) Runge, E.; Gross, E. K. U. Density-Functional Theory for Time-Dependent Systems. *Phys. Rev. Lett.* **1984**, *52*, 997–1000.
- (17) Besley, N. A.; Asmuruf, F. A. Time-dependent density functional theory calculations of the spectroscopy of core electrons. *Phys. Chem. Chem. Phys.* **2010**, *12*, 12024–12039.
- (18) Akama, T.; Nakai, H. Short-time Fourier transform analysis of real-time time-dependent Hartree-Fock and time-dependent density functional theory calculations with Gaussian basis functions. *J. Chem. Phys.* **2010**, *132*, 54104.
- (19) Hedin, L. New Method for Calculating the One-Particle Green’s Function with Application to the Electron-Gas Problem. *Phys. Rev.* **1965**, *139*, A796.
- (20) Nakatsuji, H.; Hirao, K. Cluster expansion of the wavefunction. Symmetry-adapted-cluster expansion, its variational determination, and extension of open-shell orbital theory. *J. Chem. Phys.* **1978**, *68*, 2053–2065.
- (21) Nakatsuji, H. Cluster expansion of the wavefunction. Electron correlations in ground and excited states by SAC (symmetry-adapted-cluster) and SAC CI theories. *Chem. Phys. Lett.* **1979**, *67*, 329–333.
- (22) Lopata, K.; Govind, N. Modeling Fast Electron Dynamics with Real-Time Time-Dependent Density Functional Theory: Application to Small Molecules and Chromophores. *J. Chem. Theory Comput.* **2011**, *7*, 1344 – 1355.
- (23) McKechnie, S.; Booth, G. H.; Cohen, A. J.; Cole, J. M. On the accuracy of density functional theory and wave function methods for calculating vertical ionization energies. *J. Chem. Phys.* **2015**, *142*, 194114.
- (24) Faleev, S. V.; Schilfgaarde, M. v.; Kotani, T. All-Electron Self-Consistent GW Approximation: Application to Si, MnO, and NiO. *Phys. Rev. Lett.* **2004**, *93*, 126406.
- (25) Schilfgaarde, M. v.; Kotani, T.; Faleev, S. V. Quasiparticle Self-Consistent GW Theory. *Phys. Rev. Lett.* **2006**, *96*, 226402.
- (26) Reining, L. The GW approximation: content, successes and limitations. *WIREs Comput. Mol. Sci.* **2017**, *8*, e1344.
- (27) Linderberg, J.; Öhrn, Y. *Propagators in quantum chemistry*; John Wiley & Sons, 2004.

- (28) Binkley, J. S.; Pople, J. A. Møller–Plesset theory for atomic ground state energies. *Int. J. Quantum Chem.* **1975**, *9*, 229–236.
- (29) Bartlett, R. J. Many-Body Perturbation Theory and Coupled Cluster Theory for Electron Correlation in Molecules. *Annu. Rev. Phys. Chem.* **1981**, *32*, 359 – 401.
- (30) Pulay, P.; Saebø, S. Orbital-invariant formulation and second-order gradient evaluation in Møller–Plesset perturbation theory. *Theor. Chim. Acta* **1986**, *69*, 357–368.
- (31) Knowles, P. J.; Andrews, J. S.; Amos, R. D.; Handy, N. C.; Pople, J. A. Restricted Møller–Plesset theory for open-shell molecules. *Chem. Phys. Lett.* **1991**, *186*, 130–136.
- (32) Hirao, K. Multireference Møller–Plesset method. *Chem. Phys. Lett.* **1992**, *190*, 374–380.
- (33) Murphy, R. B.; Messmer, R. P. Generalized Møller–Plesset and Epstein–Nesbet perturbation theory applied to multiply bonded molecules. *J. Chem. Phys.* **1992**, *97*, 4170–4184.
- (34) Zaitsevskii, A.; Malrieu, J. P. Multipartitioning quasidegenerate perturbation theory. A new approach to multireference Møller–Plesset perturbation theory. *Chem. Phys. Lett.* **1995**, *233*, 597–604.
- (35) Andersson, K.; Malmqvist, P.; Roos, B. O. Second-order perturbation theory with a complete active space self-consistent field reference function. *J. Chem. Phys.* **1998**, *96*, 1218.
- (36) Angeli, C.; Cimiraglia, R.; Evangelisti, S.; Leininger, T.; Malrieu, J. P. Introduction of n-electron valence states for multireference perturbation theory. *J. Chem. Phys.* **2001**, *114*, 10252.
- (37) Ghigo, G.; Roos, B. O.; Malmqvist, P. A. A modified definition of the zeroth-order Hamiltonian in multiconfigurational perturbation theory (CASPT2). *Chem. Phys. Lett.* **2004**, *396*, 142–149.
- (38) Shavitt, I.; Redmon, L. T. Quasidegenerate perturbation theories. A canonical van Vleck formalism and its relationship to other approaches. *J. Chem. Phys.* **2008**, *73*, 5711.
- (39) Granovsky, A. A. Extended multi-configuration quasi-degenerate perturbation theory: The new approach to multi-state multi-reference perturbation theory. *J. Chem. Phys.* **2011**, *134*, 214113.
- (40) Chen, Z.; Chen, X.; Ying, F.; Gu, J.; Zhang, H.; Wu, W. Nonorthogonal orbital based n-body reduced density matrices and their applications to valence bond theory. III. Second-order perturbation theory using valence bond self-consistent field function as reference. *J. Chem. Phys.* **2014**, *141*, 134118.
- (41) Sharma, S.; Jeanmairet, G.; Alavi, A. Quasidegenerate perturbation theory using matrix product states. *J. Chem. Phys.* **2016**, *144*, 034103.
- (42) Sokolov, A. Y.; Chan, G. K. L. A time-dependent formulation of multi-reference perturbation theory. *J. Chem. Phys.* **2016**, *144*, 064102.
- (43) Lischka, H.; Shepard, R.; Brown, F. B.; Shavitt, I. New implementation of the graphical unitary group approach for multireference direct configuration interaction calculations. *Int. J. Quantum Chem.* **1981**, *20*, 91–100.
- (44) Knowles, P. J.; Handy, N. C. A new determinant-based full configuration interaction method. *Chem. Phys. Lett.* **1984**, *111*, 315–321.
- (45) Sherrill, C. D.; Schaefer, H. F. The Configuration Interaction Method: Advances in Highly Correlated Approaches. *Adv. Quantum Chem.* **1999**, *34*, 143–269.
- (46) Werner, H.-J.; Kállay, M.; Gauss, J. The barrier height of the F+H₂ reaction revisited: Coupled-cluster and multireference configuration-interaction benchmark calculations. *J. Chem. Phys.* **2008**, *128*, 034305.
- (47) Shamasundar, K. R.; Knizia, G.; Werner, H. J. A new internally contracted

- multi-reference configuration interaction method. *J. Chem. Phys.* **2011**, *135*, 054101.
- (48) Stanton, J. F.; Bartlett, R. J. The equation of motion coupled-cluster method. A systematic biorthogonal approach to molecular excitation energies, transition probabilities, and excited state properties. *J. Chem. Phys.* **1993**, *98*, 7029–7039.
- (49) Chattopadhyay, S.; Mahapatra, U. S.; Mukherjee, D. Development of a linear response theory based on a state-specific multi-reference coupled cluster formalism. *J. Chem. Phys.* **2000**, *112*, 7939 – 7952.
- (50) Nayak, M. K.; Chaudhuri, R. K.; Chattopadhyay, S.; Mahapatra, U. S. Applications of core-valence extensive multi-reference coupled cluster theory and core-extensive coupled cluster-based linear response theory. *J. Mol. Struct. TheoChem* **2006**, *768*, 133 – 140.
- (51) Crawford, T. D.; Schaefer, H. F. An Introduction to Coupled Cluster Theory for Computational Chemists. **2007**, 33–136.
- (52) Shavitt, I.; Bartlett, R. J. *Many-Body Methods in Chemistry and Physics: MBPT and Coupled-Cluster Theory*; Cambridge Molecular Science; Cambridge University Press, 2009.
- (53) Datta, D.; Kong, L.; Nooijen, M. A state-specific partially internally contracted multi-reference coupled cluster approach. *J. Chem. Phys.* **2011**, *134*, 214116.
- (54) Evangelista, F. A. Alternative single-reference coupled cluster approaches for multi-reference problems: The simpler, the better. *J. Chem. Phys.* **2011**, *134*, 224102 – 224102–13.
- (55) Evangelista, F. A.; Gauss, J. An orbital-invariant internally contracted multi-reference coupled cluster approach. *J. Chem. Phys.* **2011**, *134*, 114102.
- (56) Henderson, T. M.; Bulik, I. W.; Stein, T.; Scuseria, G. E. Seniority-based coupled cluster theory. *J. Chem. Phys.* **2014**, *141*, 244104.
- (57) Eriksen, J. J.; Baudin, P.; Ettenhuber, P.; Kristensen, K.; Kjærgaard, T.; Jørgensen, P. Linear-Scaling Coupled Cluster with Perturbative Triple Excitations: The Divide–Expand–Consolidate CCSD(T) Model. *J. Chem. Theory Comput.* **2015**, 150610131843004.
- (58) Garniron, Y.; Giner, E.; Malrieu, J.-P.; Scemama, A. Alternative definition of excitation amplitudes in multi-reference state-specific coupled cluster. *J. Chem. Phys.* **2017**, *146*, 154107.
- (59) Yanai, T.; Nakajima, T.; Ishikawa, Y.; Hirao, K. A new computational scheme for the Dirac–Hartree–Fock method employing an efficient integral algorithm. *J. Chem. Phys.* **2001**, *114*, 6526–6538.
- (60) Schwarz, W. H. *Challenges Adv. Comput. Chem. Phys.*; 2010; Vol. 10; pp 1–62.
- (61) Fleig, T. Invited review: Relativistic wavefunction based electron correlation methods. *Chem. Phys.* **2012**, *395*, 2–15.
- (62) Pyykkö, P. Relativistic Effects in Chemistry: More Common Than You Thought. *Ann. Rev. Phys. Chem.* **2012**, *63*, 45–64.
- (63) Hess, B. A. Relativistic electronic-structure calculations employing a two-component no-pair formalism with external-field projection operators. *Phys. Rev. A* **1986**, *33*, 3742.
- (64) Jensen, H. J. A.; Dyllal, K. G.; Saue, T.; Fægri, K. Relativistic four-component multiconfigurational self-consistent-field theory for molecules: Formalism. *J. Chem. Phys.* **1996**, *104*, 4083–4097.
- (65) Fleig, T.; Olsen, J.; Marian, C. M. The generalized active space concept for the relativistic treatment of electron correlation. I. Kramers-restricted two-component configuration interaction. *J. Chem. Phys.* **2001**, *114*, 4775–4790.
- (66) Liu, W. Ideas of relativistic quantum chemistry. *Mol. Phys.* **2010**, *108*, 1679–1706.
- (67) Saue, T. Relativistic Hamiltonians for Chemistry : A Primer. *Chem. Phys. Chem.* **2011**, *12*, 3077–3094.

- (68) Reiher, M.; Wolf, A. Exact decoupling of the Dirac Hamiltonian. II. The generalized Douglas–Kroll–Hess transformation up to arbitrary order. *J. Chem. Phys.* **2004**, *121*, 10945.
- (69) Kutzelnigg, W. Solved and unsolved problems in relativistic quantum chemistry. *Chem. Phys.* **2012**, *395*, 16–34.
- (70) Ganyushin, D.; Neese, F. A fully variational spin-orbit coupled complete active space self-consistent field approach: Application to electron paramagnetic resonance g-tensors. *J. Chem. Phys.* **2013**, *138*, 104113.
- (71) Hu, H.; Jenkins, A. J.; Liu, H.; Kasper, J. M.; Frisch, M. J.; Li, X. Relativistic Two-Component Multireference Configuration Interaction Method with Tunable Correlation Space. *J. Chem. Theory Comput.* **2020**, *16*, 2975–2984.
- (72) Vallet, V.; Maron, L.; Teichteil, C.; Flament, J. P. A two-step uncontracted determinantal effective Hamiltonian-based SO–CI method. *J. Chem. Phys.* **2000**, *113*, 1391–1402.
- (73) Fedorov, D. G.; Finley, J. P. Spin-orbit multireference multistate perturbation theory. *Phys. Rev. A* **2001**, *64*, 042502.
- (74) Roos, B. O.; Malmqvist, P. Relativistic quantum chemistry: the multiconfigurational approach. *Phys. Chem. Chem. Phys.* **2004**, *6*, 2919–2927.
- (75) Kleinschmidt, M.; Tatchen, J.; Marian, C. M. SPOCK.CI: A multireference spin-orbit configuration interaction method for large molecules. *J. Chem. Phys.* **2006**, *124*, 124101.
- (76) Mai, S.; Müller, T.; Plasser, F.; Marquetand, P.; Lischka, H.; González, L. Perturbational treatment of spin-orbit coupling for generally applicable high-level multireference methods. *J. Chem. Phys.* **2014**, *141*, 074105.
- (77) Cheng, L.; Gauss, J. Perturbative treatment of spin-orbit coupling within spin-free exact two-component theory. *J. Chem. Phys.* **2014**, *141*, 164107.
- (78) Meitei, O. R.; Houck, S. E.; Mayhall, N. J. Spin-Orbit Matrix Elements for a Combined Spin-Flip and IP/EA approach. *J. Chem. Theory Comput.* **2020**, *16*, 3597–3606.
- (79) Majumder, R.; Sokolov, A. Y. Consistent Second-Order Treatment of Spin-Orbit Coupling and Dynamic Correlation in Quasidenerate N-Electron Valence Perturbation Theory. *J. Chem. Theory Comput.* **2024**, *20*, 4676–4688.
- (80) Sokolov, A. Y. Multi-reference algebraic diagrammatic construction theory for excited states: General formulation and first-order implementation. *J. Chem. Phys.* **2018**, *149*.
- (81) Sokolov, A. Y. Multireference perturbation theories based on the Dyall Hamiltonian. *Adv. Quantum Chem.* **2024**, *90*, 121–155.
- (82) Chatterjee, K.; Sokolov, A. Y. Second-Order Multireference Algebraic Diagrammatic Construction Theory for Photoelectron Spectra of Strongly Correlated Systems. *J. Chem. Theory Comput.* **2019**, *15*, 5908–5924.
- (83) Chatterjee, K.; Sokolov, A. Y. Extended Second-Order Multireference Algebraic Diagrammatic Construction Theory for Charged Excitations. *J. Chem. Theo. Comp.* **2020**, *16*, 6343–6357.
- (84) Mazin, I. M.; Sokolov, A. Y. Multireference Algebraic Diagrammatic Construction Theory for Excited States: Extended Second-Order Implementation and Benchmark. *J. Chem. Theory Comput.* **2021**, *17*, 6152–6165.
- (85) De Moura, C. E.; Sokolov, A. Y. Simulating X-ray photoelectron spectra with strong electron correlation using multireference algebraic diagrammatic construction theory. *Phys. Chem. Chem. Phys.* **2022**, *24*, 4769–4784.
- (86) Mazin, I. M.; Sokolov, A. Y. Core-Excited States and X-ray Absorption Spectra from Multireference Algebraic Diagrammatic Construction Theory. *J. Chem. Theo. Comp.* **2023**, *19*, 4991–5006.

- (87) Gaba, N. P.; de Moura, C. E.; Majumder, R.; Sokolov, A. Y. Simulating transient X-ray photoelectron spectra of Fe(CO) 5 and its photodissociation products with multireference algebraic diagrammatic construction theory. *Phys. Chem. Chem. Phys.* **2024**, *26*, 15927–15938.
- (88) de Moura, C. E.; Sokolov, A. Y. Efficient Spin-Adapted Implementation of Multireference Algebraic Diagrammatic Construction Theory. I. Core-Ionized States and X-ray Photoelectron Spectra. *J. Phys. Chem. A* **2024**, *128*, 5816–5831.
- (89) Schirmer, J. Beyond the random-phase approximation: A new approximation scheme for the polarization propagator. *Phys. Rev. A* **1982**, *26*, 2395–2416.
- (90) Schirmer, J.; Cederbaum, L. S.; Walter, O. New approach to the one-particle Green’s function for finite Fermi systems. *Phys. Rev. A* **1983**, *28*, 1237–1259.
- (91) Schirmer, J. Closed-form intermediate representations of many-body propagators and resolvent matrices. *Phys. Rev. A* **1991**, *43*, 4647–4659.
- (92) Mertins, F.; Schirmer, J. Algebraic propagator approaches and intermediate-state representations. I. The biorthogonal and unitary coupled-cluster methods. *Phys. Rev. A* **1996**, *53*, 2140–2152.
- (93) Trofimov, A. B.; Krivdina, I. L.; Weller, J.; Schirmer, J. Algebraic-diagrammatic construction propagator approach to molecular response properties. *Chem. Phys.* **2006**, *329*, 1–10.
- (94) Dreuw, A.; Wormit, M. The algebraic diagrammatic construction scheme for the polarization propagator for the calculation of excited states. *Wiley Interdiscip. Rev. Comput. Mol. Sci.* **2015**, *5*, 82–95.
- (95) Dempwolff, A. L.; Schneider, M.; Hodecker, M.; Dreuw, A. Efficient implementation of the non-Dyson third-order algebraic diagrammatic construction approximation for the electron propagator for closed- and open-shell molecules. *J. Chem. Phys.* **2019**, *150*, 064108.
- (96) Dempwolff, A. L.; Paul, A. C.; Belogolova, A. M.; Trofimov, A. B.; Dreuw, A. Intermediate state representation approach to physical properties of molecular electron-detached states. II. Benchmarking. *J. Chem. Phys.* **2020**, *152*, 024125.
- (97) Dempwolff, A. L.; Belogolova, A. M.; Trofimov, A. B.; Dreuw, A. Intermediate state representation approach to physical properties of molecular electron-attached states: Theory, implementation, and benchmarking. *J. Chem. Phys.* **2021**, *154*, 074105.
- (98) Banerjee, S.; Sokolov, A. Y. Algebraic Diagrammatic Construction Theory for Simulating Charged Excited States and Photoelectron Spectra. *Cite This J. Chem. Theory Comput* **2023**, *19*, 3053.
- (99) Leitner, J.; Dempwolff, A. L.; Dreuw, A. The fourth-order algebraic diagrammatic construction scheme for the polarization propagator. *J. Chem. Phys.* **2022**, *157*, 184101.
- (100) Pernpointner, M. The one-particle Green’s function method in the Dirac–Hartree–Fock framework. II. Third-order valence ionization energies of the noble gases, CO and ICN. *J. Chem. Phys.* **2004**, *121*, 8782–8791.
- (101) Pernpointner, M. The four-component two-particle propagator for the calculation of double-ionization spectra of heavy-element compounds: I. Method. *J. Phys. B At. Mol. Opt. Phys.* **2010**, *43*, 205102.
- (102) Hangleiter, A.; Pernpointner, M. The four-component two-particle propagator for the calculation of double-ionization spectra of heavy-element compounds: I. Method. *J. Phys. B At. Mol. Opt. Phys.* **2010**, *43*, 205102.
- (103) Pernpointner, M.; Visscher, L.; Trofimov, A. B. Four-Component Polarization Propagator Calculations of Electron Excitations: Spectroscopic Implications of Spin-Orbit Coupling Effects. *J. Chem. Theory Comput.* **2018**, *14*, 1510–1522.
- (104) Pernpointner, M. The relativistic polarization propagator for the calculation of electronic excitations in heavy systems. *J. Chem. Phys.* **2014**, *140*, 84108.

- (105) Krauter, C. M.; Schimmelpfennig, B.; Pernpointner, M.; Dreuw, A. Algebraic diagrammatic construction for the polarization propagator with spin-orbit coupling. *Chem. Phys.* **2017**, *482*, 286–293.
- (106) Chakraborty, S.; Mukhopadhyay, T.; Nayak, M. K.; Dutta, A. K. A relativistic third-order algebraic diagrammatic construction theory for electron detachment, attachment and excitation problems. 2024; <https://arxiv.org/abs/2405.08085>.
- (107) Breit, G. Dirac’s Equation and the Spin-Spin Interactions of Two Electrons. *Phys. Rev.* **1932**, *39*, 616–624.
- (108) Bearpark, M. J.; Handy, N. C.; Palmieri, P.; Tarroni, R. Molecular Physics An International Journal at the Interface Between Chemistry and Physics Spin-orbit interactions from self consistent field wavefunctions Spin-orbit interactions from self consistent field wavefunctions. *Mol. Phys.* **1993**, *80*, 479–502.
- (109) Berning, A.; Schweizer, M.; Werner, H.-J.; Knowles, P. J.; Palmieri, P. Spin-orbit matrix elements for internally contracted multireference configuration interaction wavefunctions Spin-orbit matrix elements for internally contracted mult. *Mol. Phys.* **2000**, *98*, 1823–1833.
- (110) Li, Z.; Xiao, Y.; Liu, W. On the spin separation of algebraic two-component relativistic Hamiltonians. *J. Chem. Phys.* **2012**, *137*, 154114.
- (111) Li, Z.; Xiao, Y.; Liu, W. On the spin separation of algebraic two-component relativistic Hamiltonians: Molecular properties. *J. Chem. Phys.* **2014**, *141*, 054111.
- (112) Cao, Z.; Li, Z.; Wang, F.; Liu, W. Combining the spin-separated exact two-component relativistic Hamiltonian with the equation-of-motion coupled-cluster method for the treatment of spin-orbit splittings of light and heavy elements. *Phys. Chem. Chem. Phys.* **2017**, *19*, 3713–3721.
- (113) Wang, X.; Sharma, S. Relativistic Semistochastic Heat-Bath Configuration Interaction. *J. Chem. Theory Comput.* **2023**, *19*, 848–855.
- (114) Heß, B. A.; Marian, C. M.; Wahlgren, U.; Gropen, O. A mean-field spin-orbit method applicable to correlated wavefunctions. *Chem. Phys. Lett.* **1996**, *251*, 365–371.
- (115) Trofimov, A. B.; Schirmer, J. Molecular ionization energies and ground- and ionic-state properties using a non-Dyson electron propagator approach. *J. Chem. Phys.* **2005**, *123*, 144115.
- (116) Banerjee, S.; Sokolov, A. Y. Third-order algebraic diagrammatic construction theory for electron attachment and ionization energies: Conventional and Green’s function implementation. *J. Chem. Phys.* **2019**, *151*, 224112.
- (117) Cremer, D. Møller–Plesset perturbation theory: from small molecule methods to methods for thousands of atoms. *Wiley Interdiscip. Rev. Comput. Mol. Sci.* **2011**, *1*, 509–530.
- (118) Angeli, C.; Cimiraglia, R.; Malrieu, J. P. n-electron valence state perturbation theory: A spinless formulation and an efficient implementation of the strongly contracted and of the partially contracted variants. *J. Chem. Phys.* **2002**, *117*, 9138.
- (119) Angeli, C.; Bories, B.; Cavallini, A.; Cimiraglia, R. Third-order multireference perturbation theory: The n-electron valence state perturbation-theory approach. *J. Chem. Phys.* **2006**, *124*, 054108.
- (120) Dyall, K. G. The choice of a zeroth-order Hamiltonian for second-order perturbation theory with a complete active space self-consistent-field reference function. *J. Chem. Phys.* **1995**, *102*, 4909.
- (121) Douglas, M.; Kroll, N. M. Quantum electrodynamical corrections to the fine structure of helium. *Ann. Phys.* **1974**, *82*, 89–155.
- (122) Jansen, G.; Hess, B. A. Revision of the Douglas-Kroll transformation. *Phys. Rev. A* **1989**, *39*, 6016.

- (123) Liu, W. Essentials of relativistic quantum chemistry. *J. Chem. Phys.* **2020**, *152*, 180901.
- (124) Moura, C. E. V.; Sokolov, A. Y. *Prism, an implementation of electronic structure theories for simulating spectroscopic properties, for current version see <https://github.com/sokolov-group/prism>*.
- (125) Sun, Q.; Zhang, X.; Banerjee, S.; Bao, P.; Barbry, M.; Blunt, N. S.; Bogdanov, N. A.; Booth, G. H.; Chen, J.; Cui, Z. H. et al. Recent developments in the PySCF program package. *J. Chem. Phys.* **2020**, *153*, 024109.
- (126) Wang, X. *Xubwa/Socutils; github, 2022. <https://github.com/xubwa/socutils>*
- (127) Roos, B. O.; Lindh, R.; Malmqvist, P.; Veryazov, V.; Widmark, P. O. Main Group Atoms and Dimers Studied with a New Relativistic ANO Basis Set. *J. Phys. Chem. A* **2004**, *108*, 2851–2858.
- (128) Kerr, J. A. K.P. Huber and G. Herzberg, molecular spectra and molecular structure: IV constants of diatomic molecules. *Anal. Chim. Acta.* **1982**, *144*, 298.
- (129) Pollak, P.; Weigend, F. Segmented Contracted Error-Consistent Basis Sets of Double- and Triple- ζ Valence Quality for One- and Two-Component Relativistic All-Electron Calculations. *J. Chem. Theory Comput.* **2017**, *13*, 3696–3705.
- (130) Franzke, Y. J.; Spiske, L.; Pollak, P.; Weigend, F. Segmented Contracted Error-Consistent Basis Sets of Quadruple- ζ Valence Quality for One- and Two-Component Relativistic All-Electron Calculations. *J. Chem. Theory Comput.* **2020**, *16*, 5658–5674.
- (131) Scherpelz, P.; Govoni, M.; Hamada, I.; Galli, G. Implementation and Validation of Fully Relativistic GW Calculations: Spin-Orbit Coupling in Molecules, Nanocrystals, and Solids. *J. Chem. Theory Comput.* **2016**, *12*, 3523–3544.
- (132) Rohatgi, A. WebPlotDigitizer. <https://automeris.io>.
- (133) Bristow, D. J.; Bancroft, G. M.; Tse, J. S. High-resolution HeI and HeII photoelectron spectra of the zinc and cadmium dihalide valence bands. *Chem. Phys.* **1983**, *75*, 263–275.
- (134) Kettunen, J. A.; Niskanen, J.; Huttula, M.; Vapa, M.; Urpelainen, S.; Aksela, H. Electron-ion coincidence study of photofragmentation of the CdCl₂ molecule. *J. Mass Spectrom.* **2011**, *46*, 901–907.
- (135) Stephens, P. J.; Devlin, F. J.; Chabalowski, C. F.; Frisch, M. J. Ab Initio calculation of vibrational absorption and circular dichroism spectra using density functional force fields. *J. Phys. Chem.* **1994**, *98*, 11623–11627.
- (136) Peterson, K. A.; Figgen, D.; Goll, E.; Stoll, H.; Dolg, M. Systematically convergent basis sets with relativistic pseudopotentials. II. Small-core pseudopotentials and correlation consistent basis sets for the post-d group 16–18 elements. *J. Chem. Phys.* **2003**, *119*, 11113–11123.
- (137) Weigend, F.; Ahlrichs, R. Balanced basis sets of split valence, triple zeta valence and quadruple zeta valence quality for H to Rn: Design and assessment of accuracy. *Phys. Chem. Chem. Phys.* **2005**, *7*, 3297–3305.
- (138) Kerr, J. A. K.P. Huber and G. Herzberg, molecular spectra and molecular structure: IV constants of diatomic molecules. *Anal. Chim. Acta.* **1982**, *144*, 298.
- (139) Kramida, A.; Ralchenko, Y.; Reader, J.; and NIST ASD Team, NIST Atomic Spectra Database (ver. 5.10), Available <https://physics.nist.gov/asd>, National Institute of Standards and Technology, Gaithersburg, MD., 2022.
- (140) Sugar, J.; Corliss, C. *Atomic energy levels of the iron-period elements: potassium through nickel*; American Chemical Society, Washington, DC, 1985.
- (141) Koseki, S.; Matsunaga, N.; Asada, T.; Schmidt, M. W.; Gordon, M. S. Spin-Orbit Coupling Constants in Atoms and Ions of Transition Elements: Comparison of Effective Core Potentials, Model Core Potentials,

- and All-Electron Methods. *J. Phys. Chem. A* **2019**, *123*, 2325–2339.
- (142) Sugar, J.; Musgrove, A. Energy Levels of Copper, Cu I through Cu XXIX. *J. Phys. Chem. Ref. Data* **1990**, *19*, 527–616.
- (143) Pickering, J. C.; Zilio, V. New accurate data for the spectrum of neutral silver. *Eur. Phys. J. D* **2001**, *13*, 181–185.
- (144) Sansonetti, J. E.; Martin, W. C. Handbook of Basic Atomic Spectroscopic Data. *J. Phys. Chem. Ref. Data* **2005**, *34*, 1559–2259.
- (145) Abraham, V.; Harsha, G.; Zgid, D. Relativistic Fully Self-Consistent GW for Molecules: Total Energies and Ionization Potentials. *J. Chem. Theory Comput.* **2024**, *20*, 4579–4590.
- (146) Ragle, J. L.; Stenhouse, I. A.; Frost, D. C.; Mcuoweli, C. A. Valence-Shell Ionization Potentials of Halomethanes by Photoelectron Spectroscopy. I CH₃Cl, CH₃Br, CH₃I. Vibrational Frequencies and Vibronic Interaction in CH₃Br⁺ and CH₃Cl⁺. *J. Chem. Phys.* **1970**, *53*, 178–184.
- (147) Woodward, A. M.; Colson, S. D.; Chupka, W. A.; White, M. G. Vibrational analysis of the *A*- \tilde{X} photodissociation spectrum of CH₃I⁺. *J. Phys. Chem.* **1986**, *90*, 274–278.
- (148) Dobber, M. R.; Buma, W. J.; De Lange, C. A. Resonance enhanced multiphoton ionization photoelectron spectroscopy on nanosecond and picosecond time scales of Rydberg states of methyl iodide. *J. Chem. Phys.* **1993**, *99*, 836–853.
- (149) Fahr, A.; Nayak, A. K.; Kurylo, M. J. The ultraviolet absorption cross sections of CH₃I temperature dependent gas and liquid phase measurements. *Chem. Phys.* **1995**, *197*, 195–203.
- (150) Schultz, T.; Fischer, I. Two-Photon Photoelectron Spectrum of Methyl Iodide through a Dissociative Intermediate State. *J. Phys. Chem. A* **1997**, *101*, 5031–5034.
- (151) Olney, T. N.; Cooper, G.; Brion, C. E. Quantitative studies of the photoabsorption (4.5–488 eV) and photoionization (9–59.5 eV) of methyl iodide using dipole electron impact techniques. *Chem. Phys.* **1998**, *232*, 211–237.
- (152) Urban, B.; Bondybey, V. E. One-color multiphoton threshold photoelectron spectra of methyl bromide, and their comparison with methyl iodide. *J. Chem. Phys.* **2002**, *116*, 4938–4947.
- (153) Hu, C.; Pei, S.; Chen, Y. L.; Liu, K. Photoelectron Imaging of Atomic Iodine Following A-Band Photolysis of CH₃I[†]. *J. Phys. Chem. A* **2007**, *111*, 6813–6821.
- (154) Alekseyev, A. B.; Liebermann, H. P.; Buenker, R. J.; Yurchenko, S. N. An ab initio study of the CH₃I photodissociation. I. Potential energy surfaces. *J. Chem. Phys.* **2007**, *126*, 234102.
- (155) Alekseyev, A. B.; Liebermann, H. P.; Buenker, R. J. An ab initio study of the CH₃I photodissociation. II. Transition moments and vibrational state control of the I^{*} quantum yields. *J. Chem. Phys.* **2007**, *126*, 234103.
- (156) De Nalda, R.; Durá, J.; García-Vela, A.; Izquierdo, J. G.; González-Vázquez, J.; Bañares, L. A detailed experimental and theoretical study of the femtosecond A-band photodissociation of CH₃I. *J. Chem. Phys.* **2008**, *128*, 244309.
- (157) Locht, R.; Leyh, B.; Jochims, H. W.; Baumgärtel, H. Medium and high resolution vacuum UV photoabsorption spectroscopy of methyl iodide (CH₃I) and its deuterated isotopomers CD₃I and CH₂DI. A Rydberg series analysis. *Chem. Phys.* **2009**, *365*, 109–128.
- (158) Durá, J.; De Nalda, R.; Amaral, G. A.; Bañares, L. Imaging transient species in the femtosecond A-band photodissociation of CH₃I. *J. Chem. Phys.* **2009**, *131*, 134311.
- (159) Rubio-Lago, L.; García-Vela, A.; Arregui, A.; Amaral, G. A.; Bañares, L. The photodissociation of CH₃I in the red edge

- of the A -band: Comparison between slice imaging experiments and multisurface wave packet calculations. *J. Chem. Phys.* **2009**, *131*, 174309.
- (160) Locht, R.; Dehareng, D.; Hottmann, K.; Jochims, H. W.; Baumgärtel, H.; Leyh, B. The photoionization dynamics of methyl iodide (CH₃I): a joint photoelectron and mass spectrometric investigation. *J. Phys. B At. Mol. Opt. Phys.* **2010**, *43*, 105101.
- (161) Thiré, N.; Cireasa, R.; Blanchet, V.; Pratt, S. T. Time-resolved photoelectron spectroscopy of the CH₃I B1E 6s [2] state. *Phys. Chem. Chem. Phys.* **2010**, *12*, 15644–15652.
- (162) Kartakoullis, A.; Samartzis, P. C.; Kitsopoulos, T. N.; Parker, D. H. Photodissociation of methyl iodide and methyl iodide clusters at 193 nm. *J. Phys. Chem. C* **2013**, *117*, 22383–22390.
- (163) Marggi Poullain, S.; Chicharro, D. V.; González-Vázquez, J.; Rubio-Lago, L.; Bañares, L. A velocity map imaging study of the photodissociation of the methyl iodide cation. *Phys. Chem. Chem. Phys.* **2017**, *19*, 7886–7896.
- (164) Forbes, R.; De Fanis, A.; Bomme, C.; Rolles, D.; Pratt, S. T.; Powis, I.; Besley, N. A.; Simon, M.; Nandi, S.; Milosavljević, A. R.; Nicolas, C.; Bozek, J. D.; Underwood, J. G.; Holland, D. M. Photoionization of the iodine 3d, 4s, and 4p orbitals in methyl iodide. *J. Chem. Phys.* **2018**, *149*, 144302.
- (165) Forbes, R.; De Fanis, A.; Bomme, C.; Rolles, D.; Pratt, S. T.; Powis, I.; Besley, N. A.; Nandi, S.; Milosavljević, A. R.; Nicolas, C.; Bozek, J. D.; Underwood, J. G.; Holland, D. M. Auger electron angular distributions following excitation or ionization of the I 3d level in methyl iodide. *J. Chem. Phys.* **2018**, *149*, 94304.
- (166) Warne, E. M.; Downes-Ward, B.; Woodhouse, J.; Parkes, M. A.; Springate, E.; Pearcy, P. A.; Zhang, Y.; Karras, G.; Wyatt, A. S.; Chapman, R. T.; Minns, R. S. Photodissociation dynamics of methyl iodide probed using femtosecond extreme ultraviolet photoelectron spectroscopy. *Phys. Chem. Chem. Phys.* **2020**, *22*, 25695–25703.
- (167) Downes-Ward, B.; Warne, E. M.; Woodhouse, J.; Parkes, M. A.; Springate, E.; Pearcy, P. A.; Zhang, Y.; Karras, G.; Wyatt, A. S.; Chapman, R. T.; Minns, R. S. Photodissociation dynamics of methyl iodide across the A-band probed by femtosecond extreme ultraviolet photoelectron spectroscopy. *J. Phys. B At. Mol. Opt. Phys.* **2021**, *54*, 134003.
- (168) Center, O. S. Ohio Supercomputer Center. 1987; <http://osc.edu/ark:/19495/f5s1ph73>.

TOC Graphic

